Journal of Non-Newtonian Fluid Mechanics 346 (2025) 105498

Contents lists available at ScienceDirect

# Journal of Non-Newtonian Fluid Mechanics

journal homepage: www.elsevier.com/locate/jnnfm

Full length article

# Modelling viscoplastic interfacial flows inclusive of curvature effects

P.T. Griffiths [a,*], D. Xu [b], L. Davoust [c]

[a] Aston Fluids Group and School of Engineering & Innovation, Aston University, Birmingham, B4 7ET, UK

[b] Department of Mechanical and Aerospace Engineering, The Hong Kong University of Science and Technology, Clear Water Bay, Kowloon, Hong Kong Special Administrative Region of China

[c] Univ. Grenoble-Alpes, CNRS, Grenoble-INP (Institute of Engineering Univ. Grenoble Alpes), SIMAP, F-38000, Grenoble, France

ARTICLE INFO

*Keywords:*
Viscoplastic
Interfacial
Wetting/dewetting
Bi-viscosity

ABSTRACT

This study presents a theoretical and numerical investigation of interfacial flows of oxidised liquid metals in a shallow annular channel in the absence of inertial effects. For the first time, viscoplastic surface behaviour induced by oxidation is modelled using a bi-viscosity law within a framework that also accounts for interfacial curvature governed by the Young–Laplace equation. By solving a coupled bulk-surface flow system, the effects of surface rheology, contact angle, and dimensionless capillary length on surface velocity and surface shear rate profiles are quantified. Results highlight the competing influences of hydrophobicity and viscoplasticity on surface and bulk flow characteristics and demonstrate that accurate modelling of such systems necessitates inclusion of both curvature and non-Newtonian surface effects. In appropriate limits, our numerical results are validated against semi-analytical solutions. Our findings offer insights relevant to metal casting applications.

## 1. Introduction

Given the growing use of room-temperature liquid metals in; flexible electronics [1–4], electro-wetting [5], and reconfigurable metallic systems [6,7], there is a demand for the surface flow of liquid metals covered by an oxide layer to be considered within the broader context of alloy casting [8,9], metal additive manufacturing [10–12], and microfluidic applications [13,14].

In these applications, liquid metals rapidly oxidise upon exposure to ambient conditions, necessitating the development of surface flow models that go beyond classical *no-slip* or *slip* boundary assumptions. Surface rheological models that incorporate variational interfacial viscosities [15], as well as curvature effects arising from wetting phenomena [16], are required to ensure a correct physical description of the problem. Although surface tension and contact angle values are measurable for certain systems, their dependence on the oxidation state remains poorly characterised.

For room-temperature liquid metals, surface viscosity data is nearly non-existent, with rare exceptions involving oxide-covered Galinstan (Ga–In–Sn eutectic alloy) [17–19]. Due to its high sensitivity to oxidation, Galinstan serves as a relevant proxy for investigating interfacial behaviours akin to those of molten aluminium- or magnesium-based alloys. Like these alloys, Galinstan's surface rheological properties evolve in a non-trivial manner during oxidation. At low oxidation levels, Newtonian approximations may suffice. However, under moderate to severe oxidation, experimental observations suggest the emergence of viscoplastic interfacial responses.

The inherently high surface tension associated with flows of liquid metals results in the emergence of a large capillary length scale, making curvature effects integral to the development of accurate surface flow models. In addition to this, oxidation-induced ageing further alters wetting behaviour, leading to a transition from hydrophobicity to hydrophilicity.

Since the early twentieth century, numerous researchers have contributed to the development of experimental test benches designed to measure interfacial properties at both micro- and macroscopic scales (see, for example, the recent review by Jaensson et al. [20]). Harkins and Meyers [21] introduced the first surface viscometer capable of measuring surface shear viscosity through a flow driven by an interfacial pressure gradient. However, this method does not eliminate the influence of Marangoni effects. To mitigate the impact of potential surface tension gradients along the flow direction, Mannheimer and Schechter [22] proposed the classical annular viscometer configuration. In this set-up – depicted in Fig. 1 – an annular shear flow is generated at the bottom boundary by a rotating disk, while the lateral walls remain stationary.

Since the work of Mannheimer and Schechter, this technique has been widely revisited and employed to determine surface shear viscosities with ever-improved accuracy [23–30]. In many of these studies,

* Corresponding author.
*E-mail address:* p.griffiths1@aston.ac.uk (P.T. Griffiths).

https://doi.org/10.1016/j.jnnfm.2025.105498
Received 9 July 2025; Received in revised form 20 September 2025; Accepted 22 September 2025
Available online 27 September 2025
0377-0257/

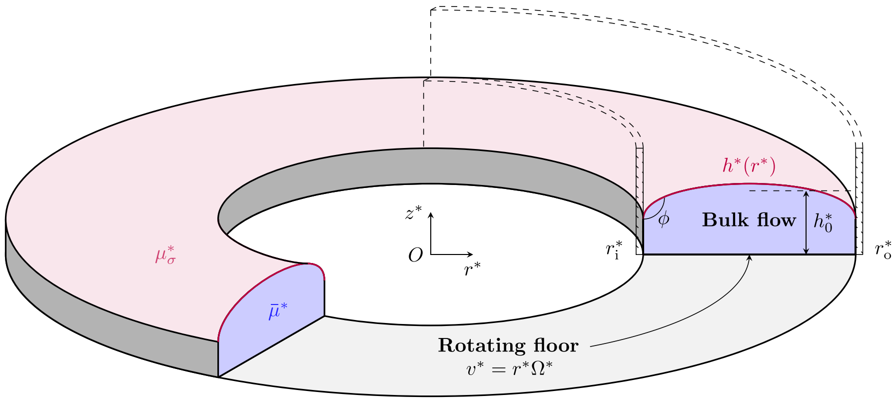


**Fig. 1.** Schematic diagram depicting the flow set-up. In this instance, we depict a hydrophobic situation ($\phi > \pi/2$). However, we will also consider the case when the fluid is wetting ($\phi < \pi/2$).

the assumption of a planar interface is adopted to significantly simplify the treatment of the tangential component of the interfacial momentum balance. This assumption is well justified when the capillary length of the fluid is much smaller than the channel width, or when the fluid wets the side walls and a sharp-edged boundary is used in conjunction with precise control of the bath height [22,31]. However, as we have previously outlined, this supposition is not justified when considering the annular flow of liquid metals.

In the present study, our investigation considers, from a theoretical point of view, the flow induced by an annular surface viscometer. Experimentally, this set-up is preferred due to the ability one has to remotely impose shear on the liquid surface through momentum diffusion from a rotating wall. To reinforce the coupling between bulk and surface dynamics, and to mimic the experimental configuration of recent associated studies [16,18], we will consider a shallow-channel geometry. Here, our investigation focuses on the surface properties of liquid metal flows, which, for the first time, necessitates accounting for viscoplastic surface behaviour resulting from the development of a surface oxidation layer. The work we present here is distinct from previous studies, in particular with respect to [32], with regards to our motivation, our formulation, and our approach to solving the problem. Here we account for viscoplastic behaviour using a bi-viscosity model, enabling us to capture yield stress effects arising from oxidation processes of liquid metals. Additionally, as opposed to using either commercially available CFD software or DNS routines, here we develop a simple numerical scheme that takes advantage of our rigorous mathematical formulation, accounting for wetting behaviour as well as non-Newtonian interfacial dynamics.

This article is outlined as follows: in Section 2 we formulate the problem, inclusive of both viscoplastic and curvature effects, in Section 3 we outline the numerical method used to solve this problem and validate this scheme in the limit when the interface is planar and Newtonian in nature, in Section 4 we present our results, and in Section 5 we draw conclusions before suggesting potential avenues for future investigations.

## 2. Problem formulation

Working in cylindrical coordinates $(r^*, \theta, z^*)$, where $^*$ denotes a dimensional quantity, we consider the steady flow of a Newtonian fluid, with viscosity $\bar{\mu}^*$, between an inner wall located at $r^* = r_\mathrm{i}^*$, and an outer wall located at $r^* = r_\mathrm{o}^*$, encased from below by the plane $z^* = 0$, and from above by the appearance of an interface that varies as a function of the radial coordinate; $z^* = h^*(r^*)$. The mean depth of the fluid inside the annular channel is denoted by $h_0^*$. In this configuration, the walls of the channel are fixed and the floor is rotated with a constant angular velocity $\Omega^*$; a schematic diagram of this flow is depicted in Fig. 1. It is assumed that the flow is steady, axisymmetric, and that the Reynolds number is small. Furthermore, the radial and wall-normal velocity components are assumed to be zero. Denoting the azimuthal flow component as $v^*$, which from this point onwards will be referred to as the bulk fluid velocity, the equation that governs the 2-D axisymmetric flow is then

$$\bar{\mu}^* \left( \nabla^2 v^* - \frac{v^*}{r^{*2}} \right) = 0. \tag{1a}$$

The boundary conditions for this problem are as follows

$$\begin{aligned} &v^*(r^* = r_\mathrm{i}^*, z^*) = v^*(r^* = r_\mathrm{o}^*, z^*) = v^*(r^*, z^* = 0) - r^*\Omega^* \\ &\quad = v^*(r^*, z^* = h^*(r^*)) - v_\sigma^* = 0, \end{aligned} \tag{1b}$$

where $v_\sigma^*$ is the fluid velocity along the surface. Throughout this article we use the subscript $\sigma^*$ in dimensional terms, and $\sigma$ in dimensionless terms, to indicate a surface quantity. The final condition stated above ensures that there is a continuity of velocity across the interface (we will use 'interface' or 'surface' interchangeably throughout this article). The exact form of $v_\sigma^*$ will be determined as part of the solution process. In order to model the effects of oxidation, which creates a rheologically distinct surface layer, we consider the emergence of a zero-thickness fluid layer with viscosity denoted by $\mu_\sigma^*$. This approach being consistent with the Gibbs framework of in-excess surface quantities [33].

A balance of the stress terms at the interface leads to the following dimensional relationship between the bulk fluid velocity and the non-Newtonian fluid velocity of the interface

$$\begin{aligned} &\underbrace{\overbrace{\mu_\sigma^* \frac{\partial}{\partial s^*}\left[\frac{1}{r^*}\frac{\partial(r^* v_\sigma^*)}{\partial s^*}\right]\bigg|_{z^*=h^*}}^{\mathrm{I}} + \overbrace{\frac{\partial \mu_\sigma^*}{\partial s^*}\left[r^* \frac{\partial}{\partial s^*}\left(\frac{v_\sigma^*}{r^*}\right)\right]\bigg|_{z^*=h^*}}^{\mathrm{II}}}_{\text{non-Newtonian surface viscous shear}} \\ &\underbrace{+ 2\mu_\sigma^* \frac{v_\sigma^*}{r^*}\frac{\mathrm{d}h^*}{\mathrm{d}r^*}\frac{\mathrm{d}^2 h^*}{\mathrm{d}r^{*2}}\left[1 + \left(\frac{\mathrm{d}h^*}{\mathrm{d}r^*}\right)^2\right]^{-2}\bigg|_{z^*=h^*}}_{\text{surface curvature}} = \underbrace{\bar{\mu}^* r^* \frac{\partial}{\partial n^*}\left(\frac{v^*}{r^*}\right)\bigg|_{z^*=h^*}}_{\text{bulk shear}}, \end{aligned} \tag{2}$$

where the tangent and normal derivatives are defined like so

$$\frac{\partial}{\partial s^*} = \left[1 + \left(\frac{\mathrm{d}h^*}{\mathrm{d}r^*}\right)^2\right]^{-1/2}\left(\frac{\partial}{\partial r^*} + \frac{\mathrm{d}h^*}{\mathrm{d}r^*}\frac{\partial}{\partial z^*}\right),$$

$$\frac{\partial}{\partial n^*} = \left[1 + \left(\frac{\mathrm{d}h^*}{\mathrm{d}r^*}\right)^2\right]^{-1/2}\left(\frac{\partial}{\partial z^*} - \frac{\mathrm{d}h^*}{\mathrm{d}r^*}\frac{\partial}{\partial r^*}\right),$$

and the non-Newtonian surface viscosity function, $\mu_\sigma^*$, is defined as follows

$$\mu_\sigma^* = \begin{cases} \mu_{\mathrm{yield}}^*, & \left| r^* \dfrac{\partial}{\partial s^*}\left(\dfrac{v_\sigma^*}{r^*}\right)\right| \le \dfrac{\tau_\mathrm{y}^*}{\mu_{\mathrm{yield}}^*}, \\ \mu^* + \tau_\mathrm{y}^*\left(1 - \dfrac{\mu^*}{\mu_{\mathrm{yield}}^*}\right)\left| r^* \dfrac{\partial}{\partial s^*}\left(\dfrac{v_\sigma^*}{r^*}\right)\right|^{-1}, & \left| r^* \dfrac{\partial}{\partial s^*}\left(\dfrac{v_\sigma^*}{r^*}\right)\right| > \dfrac{\tau_\mathrm{y}^*}{\mu_{\mathrm{yield}}^*}. \end{cases} \tag{3}$$

The first term in (2), labelled I, appears in the planar, i.e., non-curved interface, Newtonian analysis. The second term, II, appears only in the instances when the surface viscosity is a function of the surface shear rate. The non-Newtonian surface viscous shear is then defined as the sum of these two terms. The surface curvature term appears only in the instances when $h^* = h^*(r^*)$, whereas the bulk shear term appears in both the planar and non-planar analyses and depends only on bulk flow quantities. We arrive at this condition by balancing stress terms at the fluid-fluid interface. The derivation of this relationship is outlined in [34] and is motivated by the considerations of Slattery et al. [33], based on the concept of a jump momentum balance at a dividing (zero thickness) interface.

Here we adopt a bi-viscosity model, as first proposed by O'Donovan and Tanner [35], to mimic the behaviour one would observe from a Bingham constitutive law (see Fig. 2). Consistent with the Gibbs concept of an in-excess surface quantity, $\mu^*_{\text{yield}}$ is the (large) surface yield viscosity with units mass per unit time [MT$^{-1}$], i.e., it has the same dimensions as the bulk viscosity multiplied by a length scale [22]. The reference surface viscosity is $\mu^*$, and $\tau^*_{\text{y}}$ is the surface yield stress [MT$^{-2}$]. We choose to employ a regularised version of the Bingham constitutive law such that the framework we develop here can then readily be extended to any Generalised Newtonian Fluid (GNF) model. In doing so, our formulation is generic in the sense that shear-thinning or shear-thickening effects could be considered simply by appropriately adjusting the definition of the surface viscosity function $\mu^*_\sigma$. In principle, there is no reason why the classical version of the Bingham plastic law could not be applied to this problem. However, one would likely have to think carefully about how to resolve the numerical difficulties associated with the discontinuous nature of that model. Our adoption of a regularised viscosity model is therefore motivated by the ease with which it can be generalised and its amenability to numerical study.

The relative merits and drawbacks of the use of regularised models, such as O'Donovan and Tanner's bi-viscosity model, to approximate viscoplastic flow behaviour, have been discussed at length in the literature [36–38]. We will not add to that discussion here, instead, we simply make note of the recent and continued popularity of the application of such models in a range of different contexts [39–42]. To ensure that the results we present here are qualitatively independent of the choice of regularisation model, we have also considered the exponential regularisation technique first proposed by Papanastasiou [43]. Although not presented here, the nature of the results we obtain does not change between the two models. However, the clear distinction between yielded and unyielded regions becomes somewhat more difficult to assess when moving from the bi-viscosity model to Papanastasiou regularisation, this being a consequence of the exponential smoothing that is integral to the latter model.

To complete the description of the problem we must define how the function $h^*(r^*)$ is determined. The curvature of the interface, $\hat{h}^*$, is governed by the Young–Laplace equation, given as follows

$$\hat{h}^* - h_0^* = \lambda^{*2}\left\{\left[1+\left(\frac{\mathrm{d}\hat{h}^*}{\mathrm{d}r^*}\right)^2\right]^{-3/2}\frac{\mathrm{d}^2\hat{h}^*}{\mathrm{d}r^{*2}} + \left[1+\left(\frac{\mathrm{d}\hat{h}^*}{\mathrm{d}r^*}\right)^2\right]^{-1/2}\frac{1}{r^*}\frac{\mathrm{d}\hat{h}^*}{\mathrm{d}r^*}\right\}, \tag{4a}$$

where $\lambda^* = \sqrt{\gamma^*/(\rho^* g^*)}$, is the capillary length. The bulk fluid density is $\rho^*$, $g^*$ is the acceleration due to gravity, and $\gamma^*$ is the surface tension. Eq. (4a) must be solved subject to the end-point boundary conditions

$$\frac{\mathrm{d}\hat{h}^*(r^* = r_\mathrm{i}^*)}{\mathrm{d}r^*} = -\frac{\mathrm{d}\hat{h}^*(r^* = r_\mathrm{o}^*)}{\mathrm{d}r^*} = -\cot(\phi), \tag{4b}$$

where $\phi$ is the contact angle. The function $\hat{h}^*$ describes the correct interface curvature but does not account for mass conservation considerations. To account for mass conservation we note that

$$\int_{r_\mathrm{i}^*}^{r_\mathrm{o}^*} h^*\,\mathrm{d}r \equiv h_0^*(r_\mathrm{o}^* - r_\mathrm{i}^*).$$

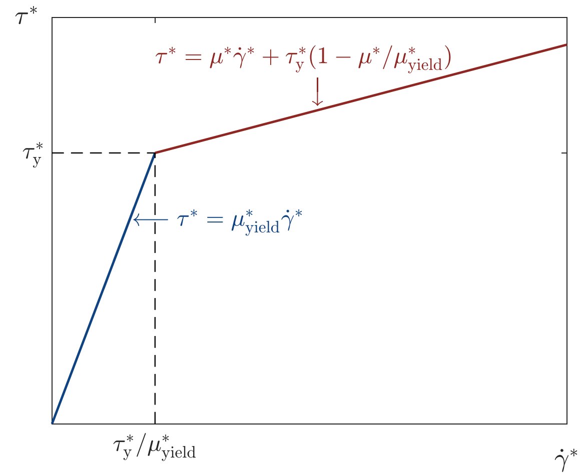


**Fig. 2.** Depiction of the bi-viscosity model used within this article. Here $\tau^*$ is shear stress and $\dot{\gamma}^*$ is shear rate; all other quantities are as per their definitions given on this page. In the limit as $\mu^*_{\text{yield}} \to \infty$, this model mimics the Bingham plastic law.

Given that $\hat{h}^*$ describes the correct curvature, then $h^*(r) \equiv \hat{h}^*(r) + \delta^*$, where $\delta^*$ accounts for an appropriate shift in the wall-normal direction to ensure that mass is conserved. Combining these two relationships, i.e., solving for $\delta^*$, one then arrives at the correct description for the variation of the curved interface:

$$h^* = h_0^* + \hat{h}^* - \frac{1}{r_\mathrm{o}^* - r_\mathrm{i}^*}\int_{r_\mathrm{i}^*}^{r_\mathrm{o}^*} \hat{h}^*\,\mathrm{d}r^*. \tag{4c}$$

Note that in the case when the interface is planar, the above is identically satisfied when $h^* = \hat{h}^* = h_0^* =$ constant.

The problem is made dimensionless as follows

$$(r_\mathrm{i}, r_\mathrm{o}, r) = \frac{(r_\mathrm{i}^*, r_\mathrm{o}^*, r^*)}{\Delta r^*}, \quad (\hat{h}, h, z) = \frac{(\hat{h}^*, h^*, z^*)}{h_0^*}, \quad (v, v_\sigma) = \frac{(v^*, v_\sigma^*)}{\Delta r^* \Omega^*},$$

where $\Delta r^* = r_\mathrm{o}^* - r_\mathrm{i}^*$, is the appropriate nondimensionalising length scale in the radial direction. It would not be correct to nondimensionalise with respect to either $r_\mathrm{i}^*$ or $r_\mathrm{o}^*$ as this would only account for the distance between the centre of the surface viscometer and the inner/outer wall, two measures that have no bearing on the flow dynamics within the channel.

The above leads to the definitions of the dimensionless numbers that govern the dynamics of this problem

$$\mathrm{Bo} = \frac{\mu^*}{\bar{\mu}^*}\frac{a_\mathrm{r}}{\Delta r^*}, \quad \mathrm{Bn} = \frac{\tau_\mathrm{y}^*}{\mu^*\Omega^*}, \quad \mu_{\text{yield}} = \frac{\mu^*_{\text{yield}}}{\mu^*}, \quad \lambda = \frac{\lambda^*}{\Delta r^*},$$

where $a_\mathrm{r} = (\Delta r^*)^{-1} h_0^*$ is the ratio of length scales, otherwise referred to as the aspect ratio. Here the Boussinesq number, Bo, describes the competition between surface and bulk viscous stresses, whereas the Bingham number, Bn, describes the competition between surface yield stress and surface viscous stress. In order to fully characterise the flow one must specify both Bo and Bn. The Boussinesq number quantifies the competition between two Couette-type mechanisms: one governed by the ability of the surface viscosity to redistribute momentum along the interface from, or towards, the lateral walls; and the other by the ability of the bulk viscosity to diffuse momentum vertically from the rotating floor up to the surface. In contrast, the Bingham number provides a measure of the tendency of the interfacial flow to overcome the yield stress induced by the oxidation process.

The dimensionless problem is thus defined like so; in the bulk, the fluid velocity is determined from the solution of the Stokes equation:

$$a_\mathrm{r}^2 \frac{\partial}{\partial r}\left[\frac{1}{r}\frac{\partial(rv)}{\partial r}\right] + \frac{\partial^2 v}{\partial z^2} = 0, \tag{5a}$$

solved subject to

$$v(r=r_{\mathrm{i}},z)=v(r=r_{\mathrm{o}},z)=v(r,z=0)-r=v(r,z=h(r))-v_{\sigma}=0. \tag{5b}$$

The function $\hat{h}(r)$ is determined from the solution of

$$\hat{h}''_{rr}=[1+(a_{\mathrm{r}}\hat{h}'_{r})^{2}]\{\lambda^{-2}(\hat{h}-1)[1+(a_{\mathrm{r}}\hat{h}'_{r})^{2}]^{1/2}-r^{-1}\hat{h}'_{r}\}, \tag{6a}$$

where a prime denotes differentiation with respect to the subscript variable. The ODE for $\hat{h}(r)$ is solved subject to the wall conditions

$$\hat{h}'_{r}(r=r_{\mathrm{i}})=-\hat{h}'_{r}(r=r_{\mathrm{o}})=-a_{\mathrm{r}}^{-1}\cot(\phi). \tag{6b}$$

The variation of the interface, $h(r)$, is then given by

$$h=1+\hat{h}-\int_{r_{\mathrm{i}}}^{r_{\mathrm{o}}}\hat{h}\,\mathrm{d}r. \tag{6c}$$

Lastly, the surface velocity, $v_\sigma$, is determined from the interfacial condition

$$\mathrm{Bo}\left\{\mu_{\sigma}\frac{\partial}{\partial s}\left[\frac{1}{r}\frac{\partial(rv_{\sigma})}{\partial s}\right]+\frac{\partial\mu_{\sigma}}{\partial s}\left[r\frac{\partial}{\partial s}\left(\frac{v_{\sigma}}{r}\right)\right]+2\mu_{\sigma}\frac{v_{\sigma}}{r}\frac{a_{\mathrm{r}}^{2}h'_{r}h''_{rr}}{[1+(a_{\mathrm{r}}h'_{r})^{2}]^{2}}\right\}\bigg|_{z=h}=r\frac{\partial}{\partial n}\left(\frac{v}{r}\right)\bigg|_{z=h}, \tag{7}$$

where

$$\frac{\partial}{\partial s}=\frac{1}{\sqrt{1+(a_{\mathrm{r}}h'_{r})^{2}}}\left(\frac{\partial}{\partial r}+h'_{r}\frac{\partial}{\partial z}\right),\quad \frac{\partial}{\partial n}=\frac{1}{\sqrt{1+(a_{\mathrm{r}}h'_{r})^{2}}}\left(\frac{\partial}{\partial z}-a_{\mathrm{r}}^{2}h'_{r}\frac{\partial}{\partial r}\right),$$

and the dimensionless non-Newtonian surface viscosity function, $\mu_\sigma$, is defined as follows

$$\mu_{\sigma}=\begin{cases}\mu_{\mathrm{yield}}, & \left|r\dfrac{\partial}{\partial s}\left(\dfrac{v_{\sigma}}{r}\right)\right|\le\dfrac{\mathrm{Bn}}{\mu_{\mathrm{yield}}},\\[2ex] 1+\mathrm{Bn}\left(1-\dfrac{1}{\mu_{\mathrm{yield}}}\right)\left|r\dfrac{\partial}{\partial s}\left(\dfrac{v_{\sigma}}{r}\right)\right|^{-1}, & \left|r\dfrac{\partial}{\partial s}\left(\dfrac{v_{\sigma}}{r}\right)\right|>\dfrac{\mathrm{Bn}}{\mu_{\mathrm{yield}}}.\end{cases} \tag{8}$$

In what follows we solve this coupled problem using a suitable numerical scheme and, in appropriate limits, we compare our numerical solutions to analytical and semi-analytical results. However, before doing so, we first provide a brief overview of how the interfacial profile is determined and how the curvature of the interface is correctly accounted for.

### 2.1. The interfacial profile

In order to solve the boundary value problem defined by (6a)–(6c) we reformulate the problem as a system of two first-order ODEs. We employ a fourth-order Runge Kutta integrator twinned with a secant method shooting scheme and a trapezoidal integrator in order to determine numerical solutions for $h(r)$ as a function of; the contact angle, the aspect ratio, and the dimensionless capillary length. The shooting method iteration ensures that our solutions are accurate to an order of at least $10^{-8}$.

In the instances when $a_{\mathrm{r}}^2 \ll 1$, an approximate analytical solution for $\hat{h}$ is obtained in terms of modified Bessel functions

$$\hat{h}\approx 1+\frac{\lambda\cot(\phi)}{a_{\mathrm{r}}C_{1,1}^{-}}\left[C_{1,0}^{+}\mathcal{I}_{0}\left(\frac{r}{\lambda}\right)+C_{0,1}^{+}\mathcal{K}_{0}\left(\frac{r}{\lambda}\right)\right],$$

where $\mathcal{I}_\nu$ and $\mathcal{K}_\nu$ are modified Bessel functions of the first and second kind, respectively, and

$$C_{p,q}^{\pm}=\mathcal{K}_{1}^{p}\left(\frac{r_{\mathrm{i}}}{\lambda}\right)\mathcal{I}_{1}^{q}\left(\frac{r_{\mathrm{o}}}{\lambda}\right)\pm\mathcal{I}_{1}^{q}\left(\frac{r_{\mathrm{i}}}{\lambda}\right)\mathcal{K}_{1}^{p}\left(\frac{r_{\mathrm{o}}}{\lambda}\right).$$

Thus, in the limit of small aspect ratio, it follows that

$$h\approx 1+\frac{\lambda\cot(\phi)}{a_{\mathrm{r}}C_{1,1}^{-}}\left\{C_{1,0}^{+}\left[\mathcal{I}_{0}\left(\frac{r}{\lambda}\right)-\Delta_{\mathcal{I}}^{-}\right]+C_{0,1}^{+}\left[\mathcal{K}_{0}\left(\frac{r}{\lambda}\right)-\Delta_{\mathcal{K}}^{+}\right]\right\}, \tag{9}$$

where $\Delta_{\mathcal{J}}^{\pm}=\Lambda_{\mathcal{J}}^{\pm}(r_{\mathrm{o}})-\Lambda_{\mathcal{J}}^{\pm}(r_{\mathrm{i}})$, and

$$\Lambda_{\mathcal{J}}^{\pm}(r)=\frac{\pi r}{2}\left[\mathcal{L}_{1}\left(\frac{r}{\lambda}\right)\mathcal{J}_{0}\left(\frac{r}{\lambda}\right)\pm\mathcal{L}_{0}\left(\frac{r}{\lambda}\right)\mathcal{J}_{1}\left(\frac{r}{\lambda}\right)\right]+r\mathcal{J}_{0}\left(\frac{r}{\lambda}\right).$$

Here $\mathcal{L}_\nu$ is the modified Struve function [44].

### 2.2. Coordinate system transformation

In what follows it is advantageous for us not to work in the $r$–$z$ coordinate system but instead in a rectangular domain. As such we define the new coordinates accordingly; $\mathcal{R}=r$, and $\mathcal{Z}=z/h(r)$. In this coordinate system derivatives with respect to $r$ and $z$ are defined like so

$$\frac{\partial}{\partial r}=\frac{\partial}{\partial\mathcal{R}}-h'_{\mathcal{R}}\frac{\mathcal{Z}}{h}\frac{\partial}{\partial\mathcal{Z}},\qquad \frac{\partial}{\partial z}=\frac{1}{h}\frac{\partial}{\partial\mathcal{Z}},$$

$$\frac{\partial^{2}}{\partial r^{2}}=\frac{\partial^{2}}{\partial\mathcal{R}^{2}}-2h'_{\mathcal{R}}\frac{\mathcal{Z}}{h}\frac{\partial^{2}}{\partial\mathcal{R}\partial\mathcal{Z}}+\left[\frac{2(h'_{\mathcal{R}})^{2}}{h}-h''_{\mathcal{R}\mathcal{R}}\right]\frac{\mathcal{Z}}{h}\frac{\partial}{\partial\mathcal{Z}}+(h'_{\mathcal{R}})^{2}\left(\frac{\mathcal{Z}}{h}\right)^{2}\frac{\partial^{2}}{\partial\mathcal{Z}^{2}},\qquad \frac{\partial^{2}}{\partial z^{2}}=\frac{1}{h^{2}}\frac{\partial^{2}}{\partial\mathcal{Z}^{2}}.$$

Thus, after making use of the definitions above, the equation that governs the bulk flow, (5a), becomes

$$(a_{\mathrm{r}}h)^{2}\frac{\partial}{\partial\mathcal{R}}\left[\frac{1}{\mathcal{R}}\frac{\partial(\mathcal{R}v)}{\partial\mathcal{R}}\right]+\frac{\partial^{2}v}{\partial\mathcal{Z}^{2}}=\underbrace{a_{\mathrm{r}}^{2}\mathcal{Z}\left(\beta_{1}\frac{\partial v}{\partial\mathcal{Z}}-\beta_{2}\mathcal{Z}\frac{\partial^{2}v}{\partial\mathcal{Z}^{2}}+2\beta_{3}\frac{\partial^{2}v}{\partial\mathcal{R}\partial\mathcal{Z}}\right)}_{\text{forcing term due to surface curvature}}, \tag{10}$$

where the $\beta_i$'s are given by

$$\beta_{1}(\mathcal{R})=\frac{hh'_{\mathcal{R}}}{\mathcal{R}}+hh''_{\mathcal{R}\mathcal{R}}-2(h'_{\mathcal{R}})^{2},\quad \beta_{2}(\mathcal{R})=(h'_{\mathcal{R}})^{2},\quad \beta_{3}(\mathcal{R})=hh'_{\mathcal{R}}.$$

These quantities constitute the forcing term due to surface curvature and appear only as a result of the coordinate system transformation. Away from the interface, the transformed boundary conditions are then

$$v(\mathcal{R}=r_{\mathrm{i}},\mathcal{Z})=0, \tag{11a}$$

$$v(\mathcal{R}=r_{\mathrm{o}},\mathcal{Z})=0, \tag{11b}$$

$$v(\mathcal{R},\mathcal{Z}=0)=\mathcal{R}. \tag{11c}$$

In the limit as $\phi\to\pi/2$, which is equivalent to the limit $h\to 1$, the $\beta_i$ functions tend to zero and we recover, identically, (5a).

### 2.3. Simplification of the interfacial condition

In order to employ the simple numerical scheme that we have developed here, we first need to describe the interfacial condition (7) in terms of derivatives with respect to $r$ and $z$, as opposed to the tangent and normal derivatives (with respect to $s$ and $n$). Having done this, we are then able to transform from the $r$–$z$ coordinate system to the $\mathcal{R}$–$\mathcal{Z}$ system as defined in Section 2.2. At this point we introduce both the bulk and surface shear rates as follows

$$\dot{\gamma}=\mathcal{R}\frac{\partial}{\partial\mathcal{R}}\left(\frac{v}{\mathcal{R}}\right),\quad \dot{\gamma}_{\sigma}=\dot{\gamma}(\mathcal{R},\mathcal{Z}=1)=\mathcal{R}\frac{\partial}{\partial\mathcal{R}}\left(\frac{v_{\sigma}}{\mathcal{R}}\right),$$

with both quantities defined solely in the $\mathcal{R}$–$\mathcal{Z}$ space.

After some lengthy algebra, that can be found in Appendix A, the condition at the interface, along the now horizontal plane $\mathcal{Z}=1$, becomes

$$\Bigg[\underbrace{a_{\mathrm{r}}^{2}h\alpha\frac{\partial v}{\partial\mathcal{Z}}+\mathrm{Bo}\,\mu_{\sigma}\frac{\partial^{2}v}{\partial\mathcal{Z}^{2}}}_{1}-\underbrace{\mathrm{Bo}(a_{\mathrm{r}}h)^{2}|\dot{\gamma}_{\sigma}|(\mu_{\sigma})'_{|\dot{\gamma}_{\sigma}|}\frac{\partial\dot{\gamma}}{\partial\mathcal{R}}}_{2}\Bigg]\Bigg|_{\mathcal{Z}=1}=\underbrace{\mathrm{Bo}\,a_{\mathrm{r}}^{2}\mu_{\sigma}\left(\beta_{1}\frac{\partial v}{\partial\mathcal{Z}}-\beta_{2}\frac{\partial^{2}v}{\partial\mathcal{Z}^{2}}+2\beta_{3}\frac{\partial^{2}v}{\partial\mathcal{R}\partial\mathcal{Z}}\right)}_{3}\Bigg|_{\mathcal{Z}=1}+a_{\mathrm{r}}^{4}h\beta_{3}\Bigg[\underbrace{\alpha\left(\dot{\gamma}-\frac{h'_{\mathcal{R}}}{h}\frac{\partial v}{\partial\mathcal{Z}}\right)}_{4}-\underbrace{\frac{\mathrm{Bo}\,h''_{\mathcal{R}\mathcal{R}}(|\dot{\gamma}_{\sigma}|\mu_{\sigma})'_{|\dot{\gamma}_{\sigma}|}}{\alpha^{2}}\dot{\gamma}}_{5}\Bigg]\Bigg|_{\mathcal{Z}=1}, \tag{11d}$$

where $\alpha(\mathcal{R}) = \sqrt{1+(a_\mathrm{r} h'_\mathcal{R})^2}$, is a measure of surface curvature (the integral of $\alpha$, with respect to $\mathcal{R}$, represents the arc length of the surface), and the surface bi-viscosity model takes the form

$$\mu_\sigma = \begin{cases} \mu_\text{yield}, & |\dot\gamma_\sigma| \le \alpha \mathrm{Bn}\,\mu_\text{yield}^{-1}, \\ 1+\alpha\mathrm{Bn}(1-\mu_\text{yield}^{-1})|\dot\gamma_\sigma|^{-1}, & |\dot\gamma_\sigma| > \alpha\mathrm{Bn}\,\mu_\text{yield}^{-1}. \end{cases} \tag{12}$$

Here we have made explicit use of the fact that $v = v_\sigma$ along the interface. Thus, all occurrences of $v_\sigma$ in (7) have been replaced with $v(\mathcal{R}, \mathcal{Z} = 1)$. However, to ensure consistency of notation, all terms that relate directly to the viscosity function have retained their $\sigma$ subscripts. Eq. (11d) therefore acts as the final boundary condition for the calculation of the bulk flow. The five terms that constitute (11d) can be understood as follows: the two expressions contained within '1' appear in the planar Newtonian analysis and represent simply the bulk shear and the Newtonian surface viscous shear, respectively. The term '2' appears only due to non-Newtonian effects, whereas the terms associated with '3' appear only due to non-planar effects. Terms '4' and '5' are apparent due to the coordinate system transformation from the $r$–$z$ space to the $\mathcal{R}$–$\mathcal{Z}$ space. They represent, respectively, a contribution from the bulk shear and a contribution from both the Newtonian and non-Newtonian surface viscous shear.

## 3. Outline of the numerical method and comparisons with known solutions

Our aim is to solve (10) subject to the four conditions (11a)–(11d). In order to motivate our choice of numerical method we focus on the simplified problem whereby the bulk flow interacts with a planar Newtonian interface ($h = \alpha = \mu_\sigma = 1$). In this limit an analytical solution exists, as was first noted by Mannheimer and Schechter [22]. In this limit, where $\mathcal{R} \equiv r$ and $\mathcal{Z} \equiv z$, we are therefore able to validate our scheme against the known exact solution.

Applying a separation of variables approach one finds that

$$v(r,z) = \sum_{n=1}^{\infty} [A_n \cosh(\kappa_n z) + B_n \sinh(\kappa_n z)]\psi_1(a_\mathrm{r}^{-1}\kappa_n r),$$

where $\psi_\nu(a_\mathrm{r}^{-1}\kappa_n r) = \mathcal{J}_\nu(a_\mathrm{r}^{-1}\kappa_n r)\mathcal{Y}_1(a_\mathrm{r}^{-1}\kappa_n r_\mathrm{i}) - \mathcal{J}_1(a_\mathrm{r}^{-1}\kappa_n r_\mathrm{i})\mathcal{Y}_\nu(a_\mathrm{r}^{-1}\kappa_n r)$, and the $\kappa_n$'s are the roots of $\psi_1(a_\mathrm{r}^{-1}\kappa_n r_\mathrm{o}) = 0$. Here $\mathcal{J}_\nu$ and $\mathcal{Y}_\nu$ are Bessel functions of the first and second kind, respectively. The constants $A_n$ and $B_n$ are given as

$$A_n = 2\frac{a_\mathrm{r}[r_\mathrm{o}^2\psi_0(a_\mathrm{r}^{-1}\kappa_n r_\mathrm{o}) - r_\mathrm{i}^2\psi_0(a_\mathrm{r}^{-1}\kappa_n r_\mathrm{i})]}{\kappa_n[r_\mathrm{i}^2\psi_0^2(a_\mathrm{r}^{-1}\kappa_n r_\mathrm{i}) - r_\mathrm{o}^2\psi_0^2(a_\mathrm{r}^{-1}\kappa_n r_\mathrm{o})]},$$
$$B_n = -A_n\frac{\mathrm{Bo}\,\kappa_n\cosh(\kappa_n) + a_\mathrm{r}^2\sinh(\kappa_n)}{\mathrm{Bo}\,\kappa_n\sinh(\kappa_n) + a_\mathrm{r}^2\cosh(\kappa_n)}.$$

Given the above expression for the flow in the bulk, the fluid velocity and shear rate along the interface are therefore given by

$$v(r, z=1) = v_\sigma = +\sum_{n=1}^{\infty} A_n \frac{a_\mathrm{r}^2\psi_1(a_\mathrm{r}^{-1}\kappa_n r)}{[\mathrm{Bo}\,\kappa_n\sinh(\kappa_n) + a_\mathrm{r}^2\cosh(\kappa_n)]},$$
$$\frac{\partial v(r,z=1)}{\partial r} - \frac{v(r,z=1)}{r} = \dot\gamma_\sigma = -\sum_{n=1}^{\infty} A_n \frac{a_\mathrm{r}\kappa_n\psi_2(a_\mathrm{r}^{-1}\kappa_n r)}{[\mathrm{Bo}\,\kappa_n\sinh(\kappa_n) + a_\mathrm{r}^2\cosh(\kappa_n)]}.$$

In order to reproduce these results numerically, we recast (the now simplified version of) (10) in terms of second-order accurate finite differences. We adopt a finite difference approach to solving the collection of problems outlined in Section 2, given that: the flow we are considering is axisymmetric and steady, the only non-zero component of the flow field is the azimuthal direction, and, after the transformation to the $\mathcal{R}$-$\mathcal{Z}$ space, we are no longer working in curvilinear coordinates. Given the relative simplicity of the bulk flow problem, this set-up naturally lends itself to a solution approach constructed via finite differences. We note that the use of such methods remains popular when solving both steady [45,46] and unsteady [47,48] viscoplastic flow problems, and also problems involving viscoelastic fluids [49,50].

**Table 1**
Comparisons between the exact analytical solutions of Mannheimer and Schechter [22] and our numerical results. In order to differentiate the solutions we denote the numerically calculated surface velocity $V_\sigma$, with $\dot\Gamma_\sigma$ the respective surface shear rate. We report the wall values of $\dot\Gamma_\sigma$ using a third-order accurate description for the first-order radial derivative. In all cases $a_\mathrm{r} = 0.25$.

| Bo | $N_\mathcal{R} = N_\mathcal{Z}$ | $\|\|v_\sigma - V_\sigma\|\|/\|\|v_\sigma\|\|$ | $\dot\gamma_\sigma(r_\mathrm{i})$ | $\dot\Gamma_\sigma(r_\mathrm{i})$ | $\dot\gamma_\sigma(r_\mathrm{o})$ | $\dot\Gamma_\sigma(r_\mathrm{o})$ |
|---|---|---|---|---|---|---|
| 0.00625 | 50 | $2.788 \times 10^{-4}$ | 4.212 | 4.214 | −4.947 | −4.953 |
| | 100 | $6.859 \times 10^{-5}$ | | 4.212 | | −4.948 |
| | 150 | $2.969 \times 10^{-5}$ | | 4.212 | | −4.947 |
| 0.06250 | 50 | $1.900 \times 10^{-4}$ | 2.869 | 2.870 | −2.850 | −2.852 |
| | 100 | $4.612 \times 10^{-5}$ | | 2.869 | | −2.850 |
| | 150 | $2.002 \times 10^{-5}$ | | 2.869 | | −2.850 |
| 0.62500 | 50 | $1.983 \times 10^{-5}$ | 0.706 | 0.707 | −0.616 | −0.617 |
| | 100 | $4.299 \times 10^{-5}$ | | 0.706 | | −0.616 |
| | 150 | $1.963 \times 10^{-6}$ | | 0.706 | | −0.616 |

If we were to account, for example, for non-zero Reynolds numbers, it is likely that we would have to move away from this solution methodology and instead adopt either finite volume or finite element approaches. Indeed, we will return to this discussion point in Section 5.

A Gauss–Seidel successive over-relaxation (SOR) scheme is thus defined as follows

$$V_{i,j}^{k+1} = (1-\omega)V_{i,j}^k + \omega\left\{\frac{(a_\mathrm{r}\delta_\mathcal{Z})^2\mathcal{R}_i[(2\mathcal{R}_i+\delta_\mathcal{R})V_{i+1,j}^k + (2\mathcal{R}_i-\delta_\mathcal{R})V_{i-1,j}^{k+1}]}{2\{2[\delta_\mathcal{R}^2 + (a_\mathrm{r}\delta_\mathcal{Z})^2]\mathcal{R}_i^2 + (a_\mathrm{r}\delta_\mathcal{R}\delta_\mathcal{Z})^2\}} + \frac{(\delta_\mathcal{R}\mathcal{R}_i)^2(V_{i,j+1}^k + V_{i,j-1}^{k+1})}{2[\delta_\mathcal{R}^2 + (a_\mathrm{r}\delta_\mathcal{Z})^2]\mathcal{R}_i^2 + (a_\mathrm{r}\delta_\mathcal{R}\delta_\mathcal{Z})^2}\right\}, \tag{13}$$

where capital letters have been used to differentiate the numerical from the analytical and $\omega$ is the relaxation factor. We discretise the domain with $N_\mathcal{R}+1$ points in the radial direction and $N_\mathcal{Z}+1$ points in the wall-normal direction. The radial and wall-normal step-sizes are therefore $\delta_\mathcal{R} = (r_\mathrm{o} - r_\mathrm{i})/N_\mathcal{R} = 1/N_\mathcal{R}$, and $\delta_\mathcal{Z} = 1/N_\mathcal{Z}$. We thus enforce (13) at all points where $2 \le i \le N_\mathcal{R}$, and $2 \le j \le N_\mathcal{Z}$. At the boundaries we have that $V_{1,j} = V_{N_\mathcal{R}+1,j} = 0$, that $V_{i,1} = \mathcal{R}_i$, and from (11d) that

$$a_\mathrm{r}^2\frac{\partial v}{\partial z} + \mathrm{Bo}\frac{\partial^2 v}{\partial z^2} = 0 \iff V_{i,N_\mathcal{Z}+1} = -\frac{c_{-p}^{(2)}\mathrm{Bo}V_{i,N_\mathcal{Z}+1-p} + \sum_{l=1}^{l=p-1}(c_{-l}^{(1)}\delta_\mathcal{Z}a_\mathrm{r}^2 + c_{-l}^{(2)}\mathrm{Bo})V_{i,N_\mathcal{Z}+1-l}}{c_0^{(1)}\delta_\mathcal{Z}a_\mathrm{r}^2 + c_0^{(2)}\mathrm{Bo}}, \tag{14}$$

where the constants $c_p^{(q)}$ represent the backward finite difference coefficients for derivatives of order ($q$) to an accuracy of $\mathcal{O}(\delta_\mathcal{Z}^{p-1})$. For example, when $p = 3$ we stipulate the condition to second-order accuracy, so that $c_0^{(1)} = 3/2$, $c_{-1}^{(1)} = -2$, $c_{-2}^{(1)} = 1/2$, and $c_0^{(2)} = 2$, $c_{-1}^{(2)} = -5$, $c_{-2}^{(2)} = 4$, $c_{-3}^{(2)} = -1$, and thus obtain

$$V_{i,N_\mathcal{Z}+1} = -\frac{-\mathrm{Bo}\,V_{i,N_\mathcal{Z}-2} + (-2\delta_\mathcal{Z}a_\mathrm{r}^2 - 5\mathrm{Bo})V_{i,N_\mathcal{Z}} + [(1/2)\delta_\mathcal{Z}a_\mathrm{r}^2 + 4\mathrm{Bo}]V_{i,N_\mathcal{Z}-1}}{(3/2)\delta_\mathcal{Z}a_\mathrm{r}^2 + 2\mathrm{Bo}}.$$

In the Newtonian limits, both planar and non-planar, we find it is sufficient to stipulate the interfacial boundary condition to this order of accuracy, i.e., to the same order to accuracy as was used to discretise the momentum equation. However, as viscoplastic effects are introduced the summation needs to be extended to ensure we arrive at fully converged solutions. This point will be discussed in more detail in the following section.

For all calculations we report here, the relaxation factor is defined to be within the range $1.5 \le \omega \le 1.9$. Given the closeness of these values to the upper limit ($\omega = 2$), we find that our solutions converge very quickly, and, given the error tolerances that we stipulate, to a high degree of precision. All results are entirely independent of the choice

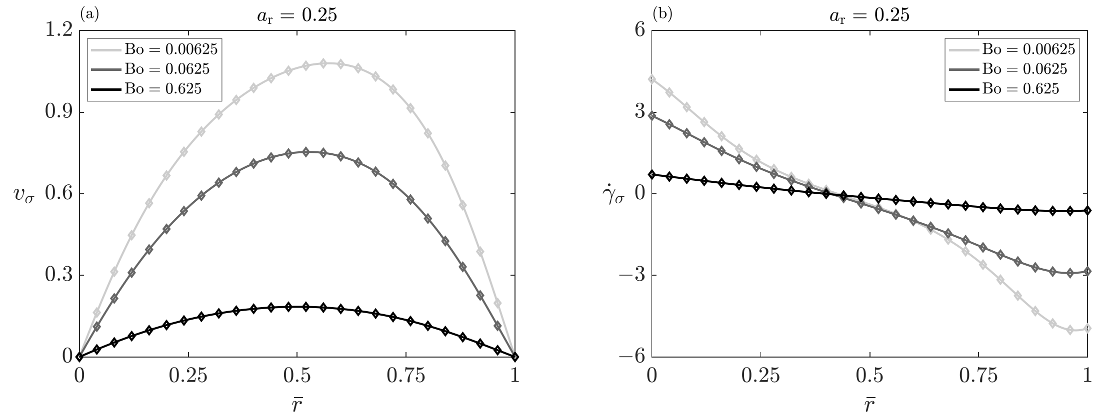


**Fig. 3.** In (a) we plot the surface velocity profiles, and in (b) we plot the surface shear rates, for three values of the Boussinesq number. The solid curves represent our numerical solutions, whereas the markers represent the known analytical solutions. The aspect ratio is fixed such that $a_r = 0.25$, and all solutions are presented as a function of $\bar{r} = r - r_i$.

of value of the relaxation factor; all that defines the choice of the value of $\omega$ is the desired speed of convergence.

Numerical testing reveals that $N_{\mathcal{R}} = N_{\mathcal{Z}} = 150$ is sufficient to obtain excellent agreement between our numerical solutions and Mannheimer & Schechter's analytical solutions (see Table 1). As part of the calculation process we stipulate two convergence criteria; the scheme iterates until $|V_{i,j}^{k+1} - V_{i,j}^{k}| < 1 \times 10^{-10}$, and the condition stipulated in (14) is also satisfied to at least the same level of precision. The agreement between these two sets of results is presented in Fig. 3 for a range of values of the Boussinesq number. In everything that follows we set $r_i^* = 30\,\mathrm{mm}$, and $r_o^* = 70\,\mathrm{mm}$, these choices are directly motivated by the experimental set-up described in [16]. Thus, the results presented in Fig. 3, where $a_r = 0.25$ (such that $h_0^* = 10\,\mathrm{mm}$, which is typical of the observations of Patouillet and Davoust [16]), represent the scenario when the reference surface viscosity is 160Bo mm times larger than the bulk viscosity. Thus when Bo $= [0.00625, 0.0625, 0.6250]$, then $\mu^*/\bar{\mu}^* = [1\,\mathrm{mm}, 10\,\mathrm{mm}, 100\,\mathrm{mm}]$. In what follows, we will focus primarily on the case when $a_r = 0.25$, and Bo $= 0.0625\,(= a_r^2)$, this being representing of the instance when the ratio of the reference surface viscosity to the bulk viscosity is equal to the wall-normal nondimensionalising length scale, $h_0^* = 10\,\mathrm{mm}$.

## 4. Results

### 4.1. Newtonian non-planar interface

It is not possible to determine an analytical solution, as per the planar work of Mannheimer and Schechter [22], in the case when the interface is non-planar in nature. However, in the instances when $a_r^2(\mathrm{d}h/\mathrm{d}r) \ll 1$ the Newtonian non-planar problem, in the $\mathcal{R}$–$\mathcal{Z}$ coordinate system, reduces significantly in complexity. The equation that describes the bulk flow is then

$$(a_r h)^2 \frac{\partial}{\partial \mathcal{R}}\left[\frac{1}{\mathcal{R}}\frac{\partial(\mathcal{R}v)}{\partial \mathcal{R}}\right] + \frac{\partial^2 v}{\partial \mathcal{Z}^2} = 0. \tag{15a}$$

In arriving at this PDE we make use of the fact, for this problem at least, that when $a_r^2(\mathrm{d}h/\mathrm{d}r)$ is small then $a_r^2(\mathrm{d}^2h/\mathrm{d}r^2)$ must also be small, i.e., $\mathrm{d}^2h/\mathrm{d}r^2$ is of the same order as $\mathrm{d}h/\mathrm{d}r$.

The above must be solved subject to

$$v(\mathcal{R} = r_i, \mathcal{Z}) = v(\mathcal{R} = r_o, \mathcal{Z}) = v(\mathcal{R}, \mathcal{Z} = 0) - \mathcal{R} = a_r^2 h \frac{\partial v(\mathcal{R}, \mathcal{Z} = 1)}{\partial \mathcal{Z}} - \mathrm{Bo}\frac{\partial^2 v(\mathcal{R}, \mathcal{Z} = 1)}{\partial \mathcal{Z}^2} = 0. \tag{15b}$$

Due to the fact that the function $h$ appears explicitly in the interfacial condition it is not possible to determine an analytical solution to this problem using a separation of variables approach. However, an

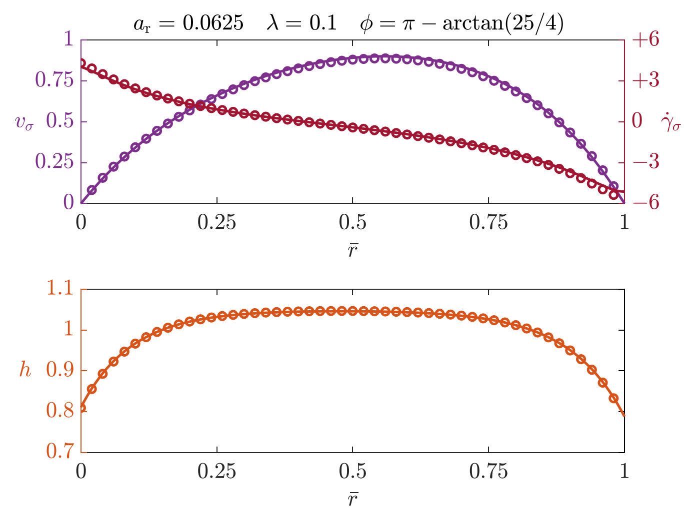


**Fig. 4.** In the top figure, we plot both the surface velocity (purple) and surface shear rate (burgundy). In the bottom figure, we plot the variation of the interface height (orange). The aspect ratio, dimensionless capillary length, and contact angle are indicated above the top figure. The Boussinesq number is fixed such that Bo = 0.0625. In all cases the solid curves represent the numerical solutions, whereas the approximate analytical results are represented by the circular markers.

*approximate* solution can be formulated at each radial location in the domain $[r_i, r_o]$. Under this approximation the surface velocity at each point $\mathcal{R}_m$ is defined as such

$$v_\sigma(\mathcal{R}_m) = \sum_{n=1}^{\infty} C_n \frac{(a_r h_m)^2 \psi_1[\kappa_n \mathcal{R}_m/(a_r h_m)]}{[\mathrm{Bo}\, h_m \kappa_n \sinh(\kappa_n) + (a_r h_m)^2 \cosh(\kappa_n)]}, \qquad \text{where} \quad h_m = h(\mathcal{R}_m),$$

for $m = 1, 2, \ldots, M$, with $\mathcal{R}_1 = r_i$, and $\mathcal{R}_M = r_o$. The constants $C_n$ are given by

$$C_n = 2\frac{a_r h_m \{r_o^2 \psi_0[\kappa_n r_o/(a_r h_m)] - r_i^2 \psi_0[\kappa_n r_i/(a_r h_m)]\}}{\kappa_n\{r_i^2 \psi_0^2[\kappa_n r_i/(a_r h_m)] - r_o^2 \psi_0^2[\kappa_n r_o/(a_r h_m)]\}},$$

with the $\kappa_n$'s being solutions of $\psi_1[\kappa_n r_o/(a_r h_m)] = 0$. The definition for the surface shear rate follows accordingly

$$\gamma_\sigma(\mathcal{R}_m) = \frac{\mathrm{d}v_\sigma(\mathcal{R}_m)}{\mathrm{d}r} - \frac{v_\sigma(\mathcal{R}_m)}{r} = -\sum_{n=1}^{\infty} C_n \frac{a_r h_m \kappa_n \psi_2[\kappa_n \mathcal{R}_m/(a_r h_m)]}{[\mathrm{Bo}\, h_m \kappa_n \sinh(\kappa_n) + (a_r h_m)^2 \cosh(\kappa_n)]}.$$

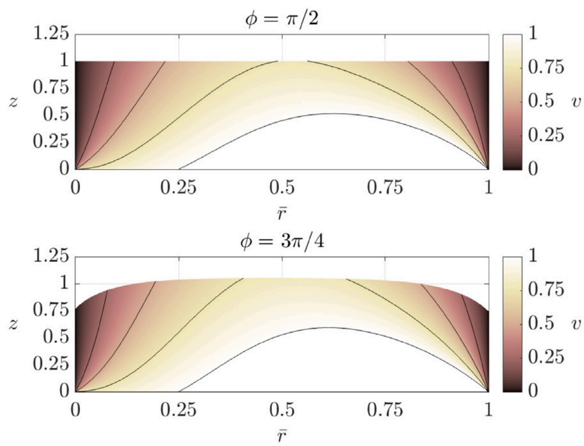

**Fig. 5.** Plots of the azimuthal velocity component for increasing values of $\phi$. The contact angle increases from left to right and down the page. In all cases the aspect ratio, Boussinesq number, and dimensionless capillary number are fixed; $a_r = 0.25$, $\mathrm{Bo} = 0.0625$, $\lambda = 0.1$.

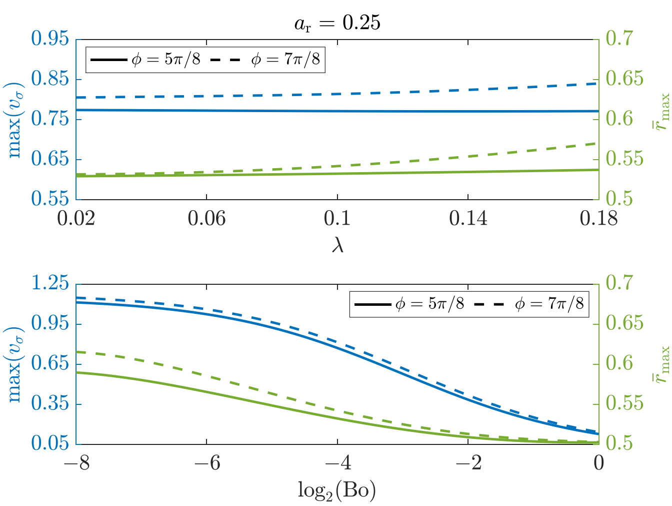

**Fig. 6.** In both figures we plot the variation of $\max(v_\sigma)$ (blue) and $\bar{r}_{\max}$ (green). In the top figure, the Boussinesq number is fixed such that $\mathrm{Bo} = 0.0625$ ($\implies \log_2(\mathrm{Bo}) = -4$), whereas in the bottom figure the dimensionless capillary length is fixed such that $\lambda = 0.1$.

Given that an approximate analytical solution for $h$ exists in the instances when $a_r^2 \ll 1$ (see Section 2.1), we are able to construct entirely analytical approximations to our numerical results in the instances when $a_r^2(\mathrm{d}h/\mathrm{d}r) \ll 1$, given that this is a more onerous restriction.

In Fig. 4 we compare our analytical approximations to our numerical solutions in the appropriate limit. The appropriateness of the limit is ensured by noting that the maximum value of $\mathrm{d}h/\mathrm{d}r$ occurs at the walls and is thus equal to, $\max(h_r') = |a_r^{-1}\cot(\phi)|$. In Fig. 4 we have stipulated that $\phi = \pi - \arctan(25/4)$, such that $a_r^2 \max(h_r') = 0.01$, given that $a_r = 0.0625$. We observe a near-perfect agreement between our analytical approximations, denoted by the circular markers, and our numerical results, given by the solid curves. This excellent agreement, that spans a broad range of both Boussinesq number and dimensionless capillary number, serves as a mechanism to validate our numerical scheme in the non-planar regime. For the remainder of this subsection, we present numerical results only; thus, we no longer need to consider appropriate asymptotic limits.

We plot the entire flow field for a range of values of the contact angle in the instance when the dimensionless capillary length is equal to 0.1, in Fig. 5. As the contact angle is increased we observe an increase in the surface velocity, with this maximum value being attained closer to the outer wall as $\phi$ increases in value from $\phi = \pi/2$. This increase in fluid velocity is a direct consequence of the growth of the maximum absolute value of the surface shear rate with increasing contact angle. We also observe that the maximum height of the interface increases (above the plane $z = 1$ in hydrophobic cases) with increasing contact angle, as is enforced by mass conservation.

In Fig. 5 we have presented results only in the case when $\mathrm{Bo} = 0.0625$, and $\lambda = 0.1$. However, the conclusions noted above hold true for a broad range of values of the dimensionless capillary length, as is evidenced in Fig. 6 where we plot the variation of $\max(v_\sigma)$ and $\bar{r}_{\max}$ (the location at which the maximum surface velocity is attained) with both $\lambda$ and Bo, for two different contact angles. As $\lambda$ increases, for a fixed Boussinesq number, so do both $\max(v_\sigma)$ and $\bar{r}_{\max}$. This behaviour is indicative of an increase in shear rate at the outer wall. These findings are consistent across all contact angles considered here, with the effects being more pronounced as the value of $\phi$ departs further from the planar case, $\phi = \pi/2$. The converse is true as Bo increases, for a fixed dimensionless capillary length. Both $\max(v_\sigma)$ and $\bar{r}_{\max}$ decrease in value (for a fixed contact angle), this being an indication that surface viscosity effects dominate over hydrophobic effects in this low Reynolds number regime.

Given that wettability can change significantly under the oxidation process, switching from hydrophobic to hydrophilic conditions can be of practical importance, and we therefore include equivalent hydrophilic results in Appendix C. These results would also be of particular interest if one were seeking to model, for example, the emergence of Langmuir films of lipids or proteins, for instance, atop an aqueous bulk flow. Information regarding the extensive applications of these types of flows is outlined in [20], and the interested reader is referred there for an excellent overview of interfacial rheology.

### 4.2. Non-Newtonian planar interface

We now consider the case when $\phi = \pi/2$, and $\mu_\sigma = \mu_\sigma(\dot{\gamma}_\sigma)$, i.e., the interface is planar but non-Newtonian in nature. A full description of the modifications to the numerical scheme outlined in Section 3, that are required to solve this variant of the problem, are provided in Appendix B. As is commonplace when modelling both shear-thinning and viscoplastic flows [51], we avoid the numerical difficulties associated with raising vanishingly small values to negative exponents by multiplying every term in the interfacial boundary condition by the absolute value of the surface shear rate. In addition to this, as noted previously, we must also make use of a more accurate description for the wall-normal derivatives that appear in (11d), to ensure that we arrive at fully converged solutions. In the Newtonian case studies (both planar and non-planar) it is sufficient to describe these derivatives to second-order

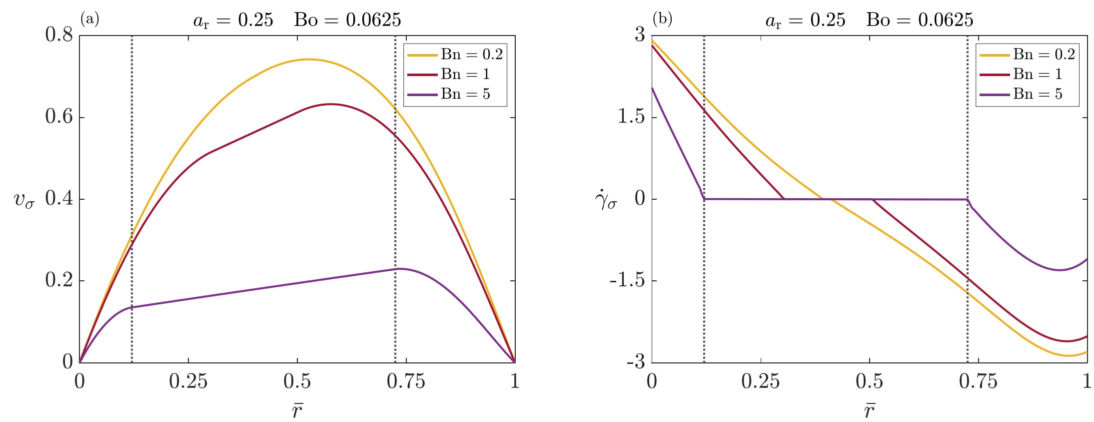


**Fig. 7.** In (a) we plot the surface velocity profiles, and in (b) we plot the surface shear rates, for three values of the Bingham number. The vertical dotted black lines indicate the extent of the unyielded region for the case when Bn = 5. In all cases $a_{\mathrm{r}} = 0.25$, and Bo = 0.0625.

accuracy ($p = 3$). However, as the magnitude of the surface yield stress grows, we determine it necessary to approximate these derivative terms to sixth-order accuracy ($p = 7$). This increase in accuracy is needed to be able to correctly account for the large gradients associated with the bi-viscosity model. For moderate values of the Bingham number such an increase in accuracy is not necessarily required. However, to ensure the consistency of the results we present here, we will report all findings given this stipulation, noting that, outside of the large Bingham number regimes, converged solutions are obtained given less accurate descriptions for the wall-normal derivatives that appear in (11d). In addition to this, we also increase, for both the planar and non-planar non-Newtonian studies, the number of discretisation points in both the radial and wall-normal directions such that $N_{\mathcal{R}} = N_{\mathcal{Z}} = 200$. In all cases, the solutions we present here are invariant upon further reducing the $\mathcal{R}$ and $\mathcal{Z}$ step-sizes. To perform the calculations in the viscoplastic regime we begin by calculating the equivalent Newtonian solution ($\mu_{\text{yield}} = 0$) and then sequentially increase the value of $\mu_{\text{yield}}$, with the previous solution being used to seed the solution at the current step. This process continues until convergence, with respect to the wall values of the surface shear rate function, has been achieved.

It is commonly noted in the literature that a value of $\mu_{\text{yield}} = 1000$ is sufficient in order to be able to accurately approximate results one would obtain from the Bingham plastic model [35,52,53]. In order to test this assertion, we have explored, for a range of Bingham numbers, the convergence of the wall values of the surface shear rate as a function of $\mu_{\text{yield}}$. These results are presented in Table 2. For moderate values of Bn, we find that our numerical solutions have converged well before the $\mu_{\text{yield}} = 1000$ threshold. It is only in the large Bingham number limit, where the unyielded region spans, say, more than approximately 50% of the annular channel width, that one needs to stipulate the value of the dimensionless surface yield viscosity to this order of magnitude. In everything that follows, we present results given a value of $\mu_{\text{yield}}$ that ensures the convergence of $\dot{\gamma}_\sigma(r_{\mathrm{o}})$ to at least 4 decimal places. In all the numerical tests we have conducted, the value of $\dot{\gamma}_\sigma(r_{\mathrm{i}})$ will have converged to at least this level of precision for a lesser value of $\mu_{\text{yield}}$. In Table 2 we also note, in the instance when Bo = 0.0625, how much of the annular channel is spanned by the unyielded region (as a percentage, accurate to 1 d.p.), with this quantity being defined as $\varrho$.

As the Bingham number is increased we observe, for example, in Fig. 7, the emergence of an unyielded zone across the annular channel where the surface shear rate is effectively zero. For any fixed value of the Boussinesq number, this solidification process serves to reduce the maximum value of the surface velocity ($\max(v_\sigma)$). In Fig. 8 we demonstrate the linear nature of the reduction in $\max(v_\sigma)$ with Bn. Twinned with this, we also predict that the maximum value of the surface velocity will shift closer to the outer wall, again in an

**Table 2**
Tabulated values of the surface shear rate function evaluated at the walls with increasing $\mu_{\text{yield}}$. We consider the low (Bn = 0.2), moderate (Bn = 1), and large (Bn = 5) Bingham number regimes, given a Boussinesq number of Bo = 0.0625. We report the wall values of $\dot{\gamma}_\sigma$ using a third-order accurate description for the first derivative. In all cases $a_{\mathrm{r}} = 0.25$.

| Bn | $\mu_{\text{yield}}$ | $\dot{\gamma}_\sigma(r_{\mathrm{i}})$ | $\dot{\gamma}_\sigma(r_{\mathrm{o}})$ | $\varrho$ |
|---|---|---|---|---|
| 0 | – | 2.869 | −2.850 | |
| 0.2 | 400 | 2.913 | −2.799 | |
| | 700 | 2.913 | −2.799 | |
| | 1000 | 2.913 | −2.799 | 2.0% |
| 1 | 600 | 2.821 | −2.514 | |
| | 800 | 2.821 | −2.514 | |
| | 1000 | 2.821 | −2.514 | 20.4% |
| 5 | 800 | 2.046 | −1.096 | |
| | 900 | 2.046 | −1.095 | |
| | 1000 | 2.046 | −1.095 | 60.7% |

almost linear fashion. The competition between surface yield stress and surface viscous stress drives the extension of the unyielded region, and thus the width of the region (measured by the quantity $\varrho$) increases monotonically with Bn.

In Fig. 9 we plot the entire flow field for a range of Bingham numbers. The flow in the bulk is strongly affected by an increase in the surface yield stress. Indeed, as Bn increases we move, gradually, towards a no-slip-like condition at the interface. This adaptation of the boundary condition results in a significant reduction in the magnitude of the flow velocity in the bulk.

In order to be able to assess how surface yield stress effects vary as a function of the competition between surface and bulk viscous stresses we plot, in Fig. 10(a), for a large range of Boussinesq numbers, the value of the Bingham number that ensures that a fixed span along the surface remains unyielded. When Bo is large, i.e., in the limit as Bo → 1, regardless of viscoplastic effects, the bulk shear at all locations along the surface is significantly diminished in magnitude (as a result $v_\sigma \approx 0$), and thus the propensity of the flow to exhibit an unyielded region is greatly enhanced. Therefore, as is evidenced in Fig. 10(a), this unyielded region will be evident for large Boussinesq number flows even for relatively small (Bn < 1) Bingham numbers.

We do not consider the case when the Boussinesq number is identically equal to zero, as this would imply a vanishing reference surface viscosity, which is clearly not physical. However, in the small Boussinesq number limit, we observe that the surface yield stress must grow progressively larger in order for the size of the unyielded region along the surface to be maintained. We do not predict asymptotic behaviour in the limit as Bo → 0, as this limit directly corresponds to the

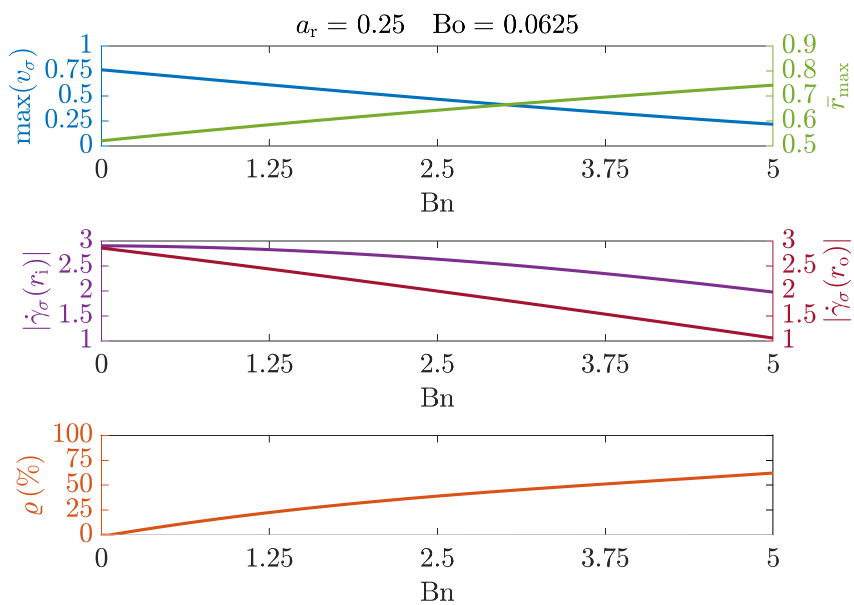


**Fig. 8.** In the top figure, we plot the variation of $\max(v_\sigma)$ (blue) and $r_{\max}$ (green) with the Bingham number. In the middle figure, we plot the variation of the absolute value of the surface shear rate at the inner (purple) and outer (burgundy) walls. In the bottom figure, we plot the variation of the quantity $\varrho$.

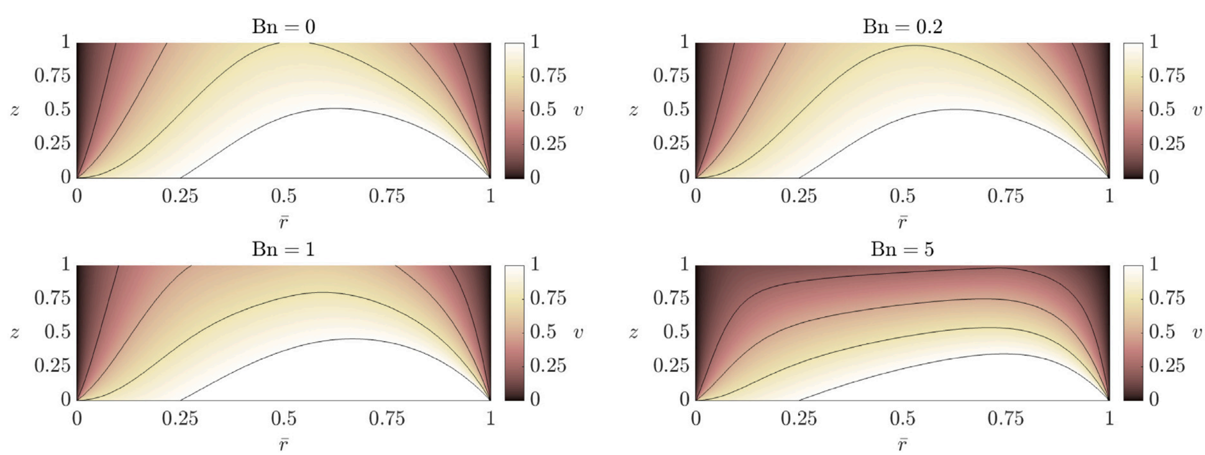


**Fig. 9.** Plots of the azimuthal velocity component for increasing values of Bn. The Bingham number increases from left to right and down the page. In all cases the aspect ratio and Boussinesq number are fixed; $a_r = 0.25$, Bo $= 0.0625$.

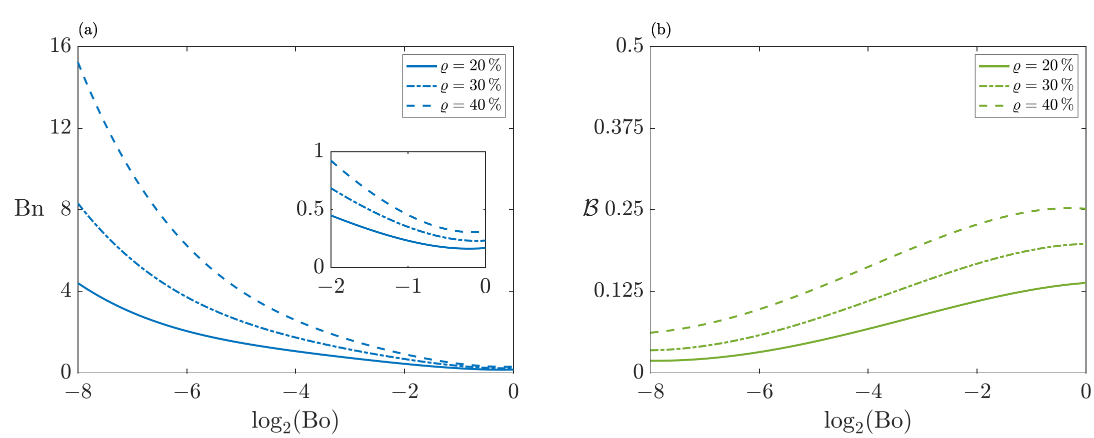


**Fig. 10.** In (a) we plot the variation of the value of the Bingham number required to ensure that a fixed width (as a percentage) of the unyielded region along the surface is maintained, as a function of the Boussinesq number. In (b) we plot the same results in terms of the effective Bingham number, $\mathcal{B}$, as opposed to the Bingham number, Bn. In both figures, the solid, dash-dotted, and dashed curves represent unyielded regions that span 20%, 30%, and 40% of the channel width, respectively.

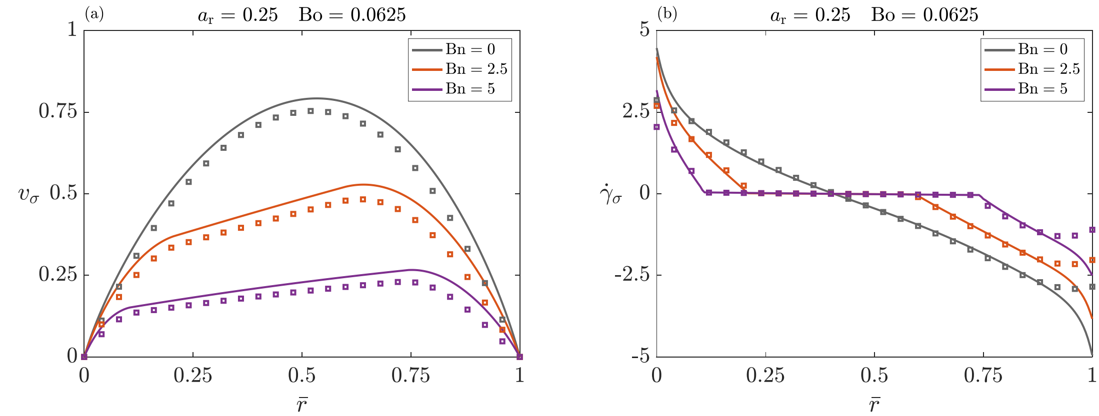


**Fig. 11.** In (a) we plot the surface velocity profiles, and in (b) we plot the surface shear rates, for three values of the Bingham number, inclusive of the Newtonian case when Bn = 0. The solid lines represent the non-planar solutions with $\phi = 3\pi/4$, and $\lambda = 0.1$. The planar results, included as a point of reference, are represented by the square markers. In all cases $a_{\rm r} = 0.25$, and Bo = 0.0625.

unphysical instance when $\mu^* \to 0$ (given that the aspect ratio must be non-zero), which, regardless of the value of the surface yield stress, implies that Bn $\to \infty$. Evidence of this singular behaviour would indeed become apparent if we were to extend the range of Boussinesq numbers we consider in Fig. 10(a).

Asymptotic behaviour is, however, recovered if the definition for the Bingham number is adjusted such that it is made independent of the reference surface viscosity. To that end, by introducing the quantity

$$\mathcal{B} = \mathrm{Bo}\,\mathrm{Bn} = \frac{\tau_{\rm y}^*}{\bar{\mu}^* \Omega^*}\frac{a_{\rm r}}{\Delta r^*},$$

we remove any dependence on $\mu^*$. The dimensionless number $\mathcal{B}$ then describes the competition between surface yield stress and bulk viscous stress, as opposed to Bn, which describes the competition between surface yield stress and surface viscous stress. If one defines the 'effective' yield stress as $\mathcal{T}_{\rm y}^* = \tau_{\rm y}^*/\Delta r^*$ (note this has the correct units for yield stress, as opposed to the surface yield stress), then we refer to $\mathcal{B} = (a_{\rm r}\mathcal{T}_{\rm y}^*)/(\bar{\mu}^*\Omega^*)$ as the 'effective' Bingham number. The plots presented in Fig. 10(a) are reproduced in Fig. 10(b), where the variation of $\varrho$ is instead considered in terms of the effective Bingham number, as opposed to Bn. Limiting behaviour in both the small and large Boussinesq number limits is evident when the results are presented in this fashion.

In what follows, we will continue to present results in terms of Bn, given that, for the sake of both consistency and brevity, we will consider only the case when Bn = 0.0625 in Section 4.3. However, we note that if further variations in important flow features were to be explored as a function of the Boussinesq number, it would likely be prudent to quantify these results in terms of $\mathcal{B}$ as opposed to Bn.

### 4.3. Non-Newtonian non-planar interface

Lastly, we consider the combination of both non-planar and non-Newtonian effects. Within this subsection, we will fix the Boussinesq number (Bn = 0.0625) and explore how variations in; the contact angle, the dimensionless capillary length, and the Bingham number affect both the bulk and surface flow characteristics. In the previous two subsections we considered how variations in the Boussinesq number affect quantities such as the maximum surface velocity and the relative size of the unyielded region. Although we do not present results for a range of Boussinesq numbers here, we can confirm that the trends previously observed, i.e., decreasing Bo increases maximum surface velocity, and, when Bo is large, the presence of an unyielded region will be apparent even for small Bingham numbers, persist when viscoplastic and non-planar effects are combined (assuming all other dimensionless control parameters are fixed).

The primary focus of the results we will present in this subsection is on the disparity in the findings one would obtain if non-planar/viscoplastic effects were not to be correctly accounted for. To that end, in Fig. 11 we present a comparison between the planar/non-planar results for surface velocity and surface shear rate in both the Newtonian (Bn = 0) and viscoplastic (Bn = 2.5, 5) regimes. As noted previously, an increase in contact angle increases the maximum surface velocity, and this finding is consistent across all Bingham numbers. Interestingly, we observe that the difference between the planar and non-planar results remains relatively constant as the Bingham number increases. This suggests that the effects of viscoplasticity do not serve to either enhance nor diminish the effects of surface curvature. Furthermore, as can be noted from Fig. 11(a) and (b), respectively, surface curvature has a very minimal effect on both the radial location of the maximum surface velocity and the relative size of the unyielded region, given a fixed value of the Bingham number. Thus, although the gradient of the surface shear rate function is significantly increased near the walls (in absolute value) as $\phi$ increases from $\phi = \pi/2$, this does not translate to a significant enough change to the bulk shear profile along the surface such that it is comparatively easier to overcome the surface yield stress. Initially, this would appear to be a rather surprising result. However, we recall that, in the non-planar cases, the Bingham number is effectively scaled by the measure of the surface curvature $\alpha$, see (12). Thus, in relative terms, the Bingham number effectively increases near to the walls, given that this is where the gradient of the curvature is the largest, and $\alpha = \sqrt{1 + (a_{\rm r} h'_{\mathcal{R}})^2}$. It is this effective dependence of the Bingham number on the surface profile that ensures that there is not a significant change in the yielded/unyielded properties of the surface flow as the contact angle increases.

To explore the consequences of not accounting for curvature and viscoplastic effects, we present, in Fig. 12, the relative difference between the hydrophobic Newtonian and non-Newtonian flow fields (column on the left), and non-Newtonian planar and non-planar flow fields (column on the right). Given the imposition of the no-slip condition along the inner and outer walls, we simply fix the relative difference there to be identically zero. Comparing planar and non-planar solutions (second column), we observe that the flow in the bulk is more strongly affected in the instances when Bn > 0. Thus, although the changes in the surface flow with increasing contact angle are relatively consistent across Bingham numbers (Fig. 11), the bulk flow is more significantly affected by viscoplasticity for a fixed hydrophobic contact angle. However, when we compare Newtonian and non-Newtonian solutions (first column), we observe that the difference between the two flow fields remains relatively consistent with increasing contact. This suggests that failing to account for surface oxidation is essentially equally as important in both the planar and non-planar cases.

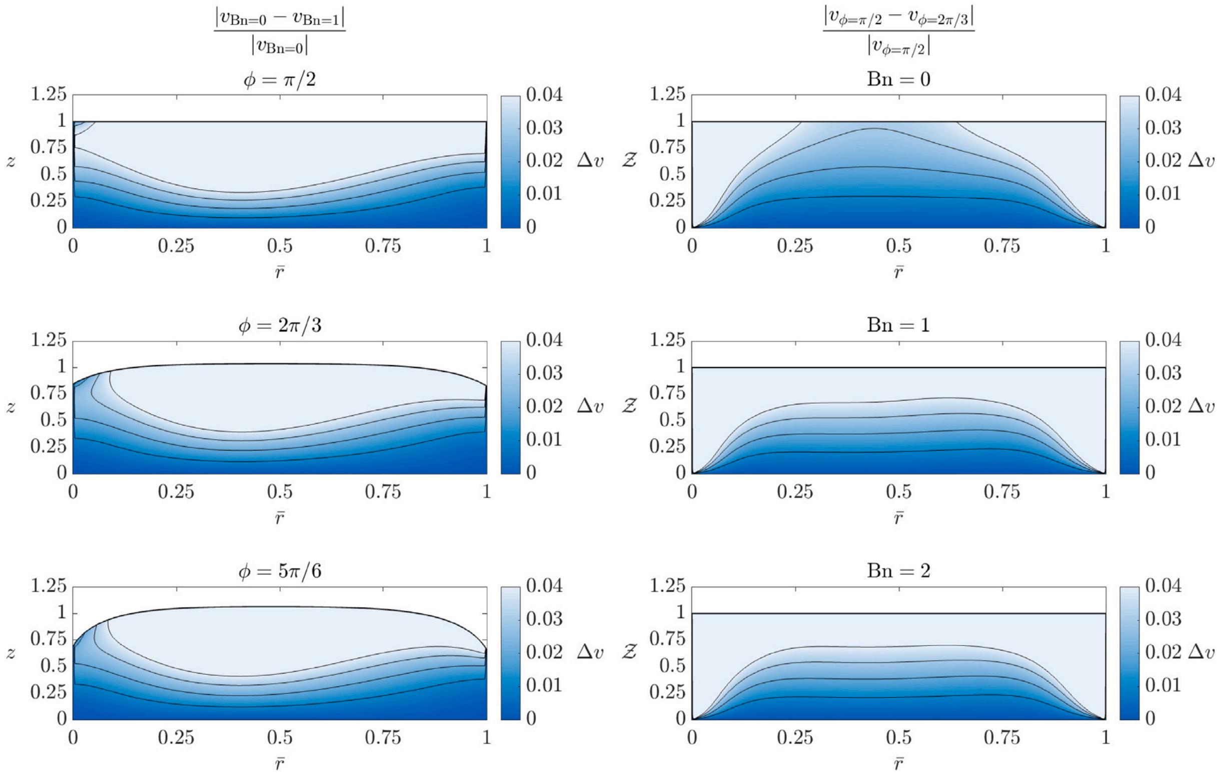


**Fig. 12.** Plots of the relative difference between the azimuthal velocity components. In the first column, the surface is considered to be Newtonian (Bn = 0) vs. non-Newtonian (Bn = 1) for a range of increasing contact angles. In the second column, the surface is considered to be planar ($\phi = \pi/2$) vs. non-planar ($\phi = 2\pi/3$) for a range of increasing Bingham numbers. The aspect ratio and Boussinesq number are fixed; $a_r = 0.25$, Bo = 0.0625, and in all non-planar cases the dimensionless capillary length is $\lambda = 0.1$.

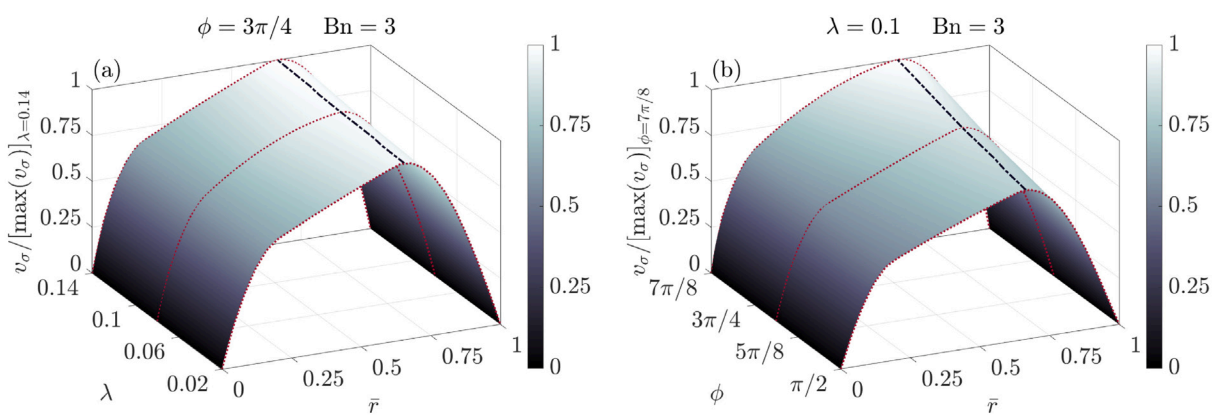


**Fig. 13.** In (a) we plot normalised surface velocity profiles for a range of values of $\lambda$ given a fixed contact angle $\phi = 3\pi/4$. The results have been normalised with respect to $\max(v_\sigma)$ in the instance when $\lambda = 0.14$. In (b) we present similar results for a range of values of $\phi$ given a fixed capillary length $\lambda = 0.1$ where, in this case, the results have been normalised with respect to $\max(v_\sigma)$ in the instance when $\phi = 7\pi/8$. In both (a) and (b) we plot the trace of the maximum normalised surface velocity contour using a dash-dotted line. The aspect ratio, Boussinesq number, and Bingham number are fixed; $a_r = 0.25$, Bo = 0.0625, Bn = 3.

In Fig. 13, we present surface velocity profiles for a fixed Bingham number (Bn = 3), across a range of dimensionless capillary lengths (a), and contact angles (b). In order to better quantify these results, each profile has been normalised by the respective maximum of $v_\sigma$ in the domain considered. For a fixed contact angle, an increase in the capillary length clearly has a very minimal effect on the surface flow, (a). However, for a fixed capillary length, an increase in the contact angle has a much more pronounced effect, (b). The results presented in Fig. 12 demonstrate the importance of differentiating planar and non-planar flows in both the Newtonian and non-Newtonian regimes. The results we present in Fig. 13 suggest that it is the correct characterisation of the contact angle that is of primary importance, given that the surface flow is largely unchanged with variations in $\lambda$. This conclusion is consistent across all Bingham numbers, including Bn = 0, as is evidenced by the results presented in Fig. 14 where we compare how the surface flow characteristics change, as a function of the Bingham number, for different contact angles (left column), and different dimensionless capillary lengths (right column). We observe that there is in fact very little variation in the size of the unyielded region upon changes in either the contact angle or the capillary length. Experimentally, it should, therefore, be possible to characterise the surface oxidation via the Bingham number simply by measuring the

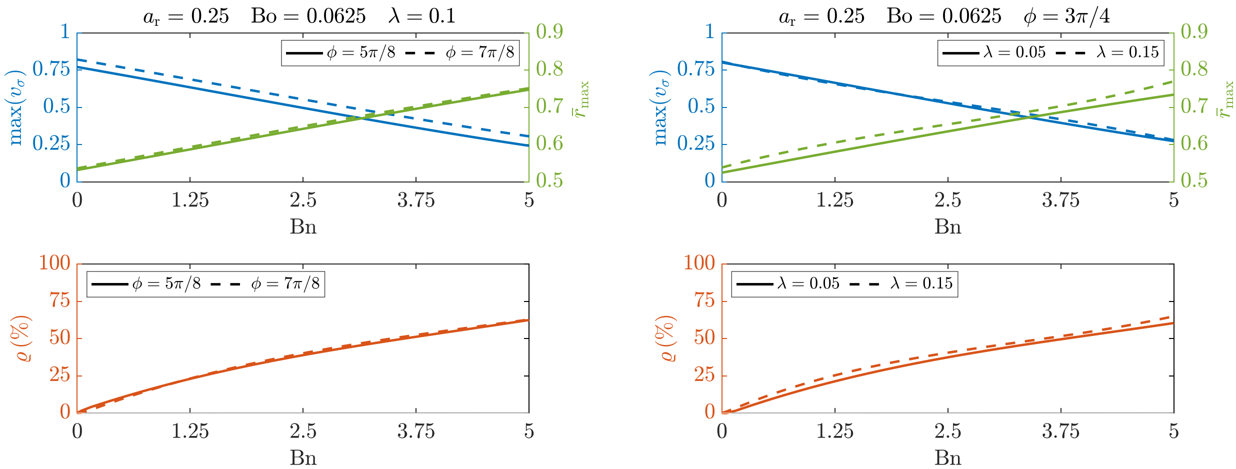


**Fig. 14.** On the left we compare the variation of $\max(v_\sigma)$, $r_{\max}$, and $\varrho$ with the Bingham number for a fixed value of $\lambda$ and two hydrophobic contact angles. On the right we compare the variation of the same quantities but in this instance fix $\phi$ and consider the cases when $\lambda = 0.05$, and $\lambda = 0.15$.

size of the unyielded region without the specific need to account for non-planar dynamics. This verification of the results we have presented here is of primary importance to us, and we expect to report on these experimental findings in due course.

## 5. Discussion and conclusions

We have developed a framework that captures surface oxidation effects in liquid metal flows. The methodology presented here is general in the sense that it could readily be extended to any Generalised Newtonian Fluid (GNF) model. Our mathematical formulation is independent of the form of the viscosity model given that the surface viscosity is a function of the surface shear rate — the definition of a GNF. This fact, twinned with the fact that our formulation is also able to account for dewetting (hydrophilic) effects, means that the model we present here would also be suitable to use when analysing condensed-phase monomolecular films atop an aqueous bulk flow, where shear-thinning effects have already been shown to be of importance [30].

In order to capture the effects of surface oxidation we have made use of O'Donovan and Tanner's bi-viscosity model to approximate viscoplastic flow behaviour. Given that the surface yield viscosity is sufficiently large, this serves as an excellent proxy to the Bingham plastic model. In much the same way as [32], we describe the curvature of the liquid metal surface via the Young–Laplace equation and, in the limit of small aspect ratio, have determined approximate analytical solutions that have been shown to be in excellent agreement to equivalent numerical results.

Our findings reveal that accounting for both non-planar and viscoplastic effects is of paramount importance in order to be able to correctly characterise liquid metal flows that exhibit surface oxidation. As surface curvature effects are enhanced we find, for a fixed Boussinesq number, that the maximum surface velocity increases and that the location of this maximum velocity shifts towards the outer wall. This being a consequence of the relative reduction in the surface shear rate at the outer wall, when compared with the inner wall, as non-planar effects become more pronounced. A similar radial shifting trend is predicted upon increasing viscoplasticity effects; however, as one would expect, the maximum surface velocity diminishes as the Bingham number increases. This reduction in the surface velocity, as a consequence of surface oxidation, has a significant retarding effect on the flow in the bulk.

In order to be able to correctly characterise flows of this nature, one must specify both the ratio of surface viscous stress to bulk viscous stress (the Boussinesq number, Bo), and the ratio of surface yield stress to surface viscous stress (the Bingham number, Bn). This is true for moderate Boussinesq numbers, however, in the limit of either very large or very small Boussinesq numbers, we find that we are able to characterise the surface flow via just the stipulation of what we have referred to as the effective Bingham number, this being the product of the Boussinesq number and the Bingham number, a quantity that is independent of a reference surface viscosity.

The methodology and results we have presented here should allow for better quantification and measurement of the shear response of oxidised liquid metal surfaces in casting processes. Although we have considered only one specific flow configuration – the annular surface viscometer – the ideas we have presented here could readily be extended to other configurations in the low Reynolds number regime.

For annular viscometer flows, it is entirely appropriate to adopt a zero Reynolds number approach, and the relatively simple numerical scheme that we have developed here makes use of this justified simplification. However, in order to explore the inclusion of both inertial and/or unsteady effects, one would likely need to move away from the finite difference formulation we have presented here and consider, instead, the use of finite element (or finite volume) schemes. Although the bulk flow is steady in nature, it would be of particular interest to conduct unsteady simulations of the surface flow, as one could then quantify how the oxidation process evolves in time. Indeed, we intend to pursue this avenue of investigation, as well as the experimental verification noted in Section 4.3, and hope to report on these findings in due course.

## CRediT authorship contribution statement

**P.T. Griffiths:** Writing – review & editing, Writing – original draft, Supervision, Project administration, Methodology, Investigation, Funding acquisition, Formal analysis, Conceptualization. **D. Xu:** Writing – review & editing, Writing – original draft, Methodology, Investigation, Formal analysis. **L. Davoust:** Writing – review & editing, Writing – original draft, Supervision, Investigation, Conceptualization.

## Declaration of competing interest

The authors declare the following financial interests/personal relationships which may be considered as potential competing interests: Paul Griffiths reports financial support was provided by Engineering and Physical Sciences Research Council. If there are other authors, they declare that they have no known competing financial interests or personal relationships that could have appeared to influence the work reported in this paper.

**Acknowledgements**

This work was supported by the Engineering and Physical Science Research Council, award number: EP/Y031644/1. The authors acknowledge the use of the High Performance Computing (HPC) facilities and the associated support services at Aston University (TAURUS HPC) in the completion of this work. SIMaP laboratory is part of the **LabEx Tec 21** (Investissements d'Avenir—Grant No. ANR-11-**LABX**-0030).

## Appendix A. Derivation of the transformed interfacial condition

We begin by rewriting the second term on the left-hand side of (7) as follows

$$\frac{\partial \mu_\sigma}{\partial s}\left[r\frac{\partial}{\partial s}\left(\frac{v_\sigma}{r}\right)\right] = \mathcal{D}\mu_\sigma \frac{\partial}{\partial s}\left[r\frac{\partial}{\partial s}\left(\frac{v_\sigma}{r}\right)\right]. \tag{A.1}$$

where

$$\mathcal{D}\mu_\sigma = \begin{cases} 0, & \left|r\dfrac{\partial}{\partial s}\left(\dfrac{v_\sigma}{r}\right)\right| \le \dfrac{\mathrm{Bn}}{\mu_{\text{yield}}}, \\ \mathrm{Bn}\left(\dfrac{1}{\mu_{\text{yield}}}-1\right), & \left|r\dfrac{\partial}{\partial s}\left(\dfrac{v_\sigma}{r}\right)\right| > \dfrac{\mathrm{Bn}}{\mu_{\text{yield}}}. \end{cases}$$

We now rewrite the partial derivative terms that appear in (7) and (A.1) with respect to $s$ and $n$, in terms of $r$ and $z$. We have that

$$r\frac{\partial}{\partial n}\left(\frac{v}{r}\right) = \frac{1}{\alpha}\left[\frac{\partial v}{\partial z} - a_\mathrm{r}^2 h_r' r\frac{\partial}{\partial r}\left(\frac{v}{r}\right)\right],$$

$$\begin{aligned}\frac{\partial}{\partial s}\left[\frac{1}{r}\frac{\partial (r v_\sigma)}{\partial s}\right] = \frac{1}{\alpha^2}\Bigg\{&\frac{\partial}{\partial r}\left[\frac{1}{r}\frac{\partial (r v_\sigma)}{\partial r}\right] + \frac{1}{r}\frac{\partial}{\partial r}\left(r h_r'\frac{\partial v_\sigma}{\partial z}\right) \\ &+ h_r'\frac{\partial}{\partial z}\left(\frac{\partial v_\sigma}{\partial r} + h_r'\frac{\partial v_\sigma}{\partial z}\right)\Bigg\} \\ &- \frac{a_\mathrm{r}^2 h_r' h_{rr}''}{\alpha^4}\left[\frac{1}{r}\frac{\partial (r v_\sigma)}{\partial r} + h_r'\frac{\partial v_\sigma}{\partial z}\right],\end{aligned}$$

$$\begin{aligned}\frac{\partial}{\partial s}\left[r\frac{\partial}{\partial s}\left(\frac{v_\sigma}{r}\right)\right] = \frac{1}{\alpha^2}\Bigg\{&\frac{\partial}{\partial r}\left[r\frac{\partial}{\partial r}\left(\frac{v_\sigma}{r}\right)\right] + \frac{1}{r}\frac{\partial}{\partial r}\left(r h_r'\frac{\partial v_\sigma}{\partial z}\right) \\ &+ h_r'\frac{\partial}{\partial z}\left(\frac{\partial v_\sigma}{\partial r} + h_r'\frac{\partial v_\sigma}{\partial z}\right)\Bigg\} \\ &- \frac{a_\mathrm{r}^2 h_r' h_{rr}''}{\alpha^4}\left[r\frac{\partial}{\partial r}\left(\frac{v_\sigma}{r}\right) + h_r'\frac{\partial v_\sigma}{\partial z}\right] - \frac{2}{\alpha^2}\frac{h_r'}{r}\frac{\partial v_\sigma}{\partial z},\end{aligned}$$

where $\alpha(\mathcal{R}) = \sqrt{1+(a_\mathrm{r} h_r')^2}$. Given the above then

$$\begin{aligned}\frac{\partial}{\partial s}\left[\frac{1}{r}\frac{\partial (r v_\sigma)}{\partial s}\right] + 2\frac{v_\sigma}{r}\frac{a_\mathrm{r}^2 h_r' h_{rr}''}{[1+(a_\mathrm{r} h_r')^2]^2} = \frac{1}{\alpha^2}\Bigg\{&\frac{\partial}{\partial r}\left[\frac{1}{r}\frac{\partial (r v_\sigma)}{\partial r}\right] + \frac{1}{r}\frac{\partial}{\partial r}\left(r h_r'\frac{\partial v_\sigma}{\partial z}\right) \\ &+ h_r'\frac{\partial}{\partial z}\left(\frac{\partial v_\sigma}{\partial r} + h_r'\frac{\partial v_\sigma}{\partial z}\right)\Bigg\} \\ &- \frac{a_\mathrm{r}^2 h_r' h_{rr}''}{\alpha^4}\left[r\frac{\partial}{\partial r}\left(\frac{v_\sigma}{r}\right) + h_r'\frac{\partial v_\sigma}{\partial z}\right].\end{aligned}$$

The interfacial condition can therefore be expressed in the following manner

$$\begin{aligned}&\mathrm{Bo}\left\{\mu_\sigma\frac{\partial}{\partial r}\left[\frac{1}{r}\frac{\partial (r v_\sigma)}{\partial r}\right] + \mathcal{D}\mu_\sigma\frac{\partial}{\partial r}\left[r\frac{\partial}{\partial r}\left(\frac{v_\sigma}{r}\right)\right] - 2\mathcal{D}\mu_\sigma\frac{h_r'}{r}\frac{\partial v_\sigma}{\partial z}\right\}\Bigg|_{z=h} \\ &\quad+\mathrm{Bo}(\mu_\sigma+\mathcal{D}\mu_\sigma)\left[\frac{1}{r}\frac{\partial}{\partial r}\left(r h_r'\frac{\partial v_\sigma}{\partial z}\right) + h_r'\frac{\partial}{\partial z}\left(\frac{\partial v_\sigma}{\partial r} + h_r'\frac{\partial v_\sigma}{\partial z}\right)\right]\Bigg|_{z=h} \\ &\quad-\mathrm{Bo}(\mu_\sigma+\mathcal{D}\mu_\sigma)\frac{a_\mathrm{r}^2 h_r' h_{rr}''}{\alpha^2}\left[r\frac{\partial}{\partial r}\left(\frac{v_\sigma}{r}\right) + h_r'\frac{\partial v_\sigma}{\partial z}\right]\Bigg|_{z=h} \\ &= \alpha\left[\frac{\partial v}{\partial z} - a_\mathrm{r}^2 h_r' r\frac{\partial}{\partial r}\left(\frac{v}{r}\right)\right]\Bigg|_{z=h}.\end{aligned} \tag{A.2}$$

Given the form of the governing bulk flow Eq. (5a), and the fact that $v = v_\sigma$ along the interface, the first term in (A.2) can be rewritten, and all explicit appearances of $v_\sigma$ can be replaced with $v$. Thus

$$\begin{aligned}&\mathrm{Bo}\left\{-\frac{\mu_\sigma}{a_\mathrm{r}^2}\frac{\partial^2 v}{\partial z^2} + \mathcal{D}\mu_\sigma\frac{\partial}{\partial r}\left[r\frac{\partial}{\partial r}\left(\frac{v}{r}\right)\right] - 2\mathcal{D}\mu_\sigma\frac{h_r'}{r}\frac{\partial v}{\partial z}\right\}\Bigg|_{z=h} \\ &\quad+\mathrm{Bo}(\mu_\sigma+\mathcal{D}\mu_\sigma)\left[\frac{1}{r}\frac{\partial}{\partial r}\left(r h_r'\frac{\partial v}{\partial z}\right) + h_r'\frac{\partial}{\partial z}\left(\frac{\partial v}{\partial r} + h_r'\frac{\partial v}{\partial z}\right)\right]\Bigg|_{z=h} \\ &\quad-\mathrm{Bo}(\mu_\sigma+\mathcal{D}\mu_\sigma)\frac{a_\mathrm{r}^2 h_r' h_{rr}''}{\alpha^2}\left[r\frac{\partial}{\partial r}\left(\frac{v}{r}\right) + h_r'\frac{\partial v}{\partial z}\right]\Bigg|_{z=h} \\ &= \alpha\left[\frac{\partial v}{\partial z} - a_\mathrm{r}^2 h_r' r\frac{\partial}{\partial r}\left(\frac{v}{r}\right)\right]\Bigg|_{z=h}.\end{aligned} \tag{A.3}$$

At this stage terms associated with the surface viscosity function are still expressed in terms of the surface velocity.

The next step is to then transform this expression for the interfacial boundary condition to the $\mathcal{R}$–$\mathcal{Z}$ coordinate system as defined in 2.2. The benefit of this transformation is that it serves to effectively 'flatten' the interface such that all points along the curved plane $z = h$, are recast along the plane $\mathcal{Z} = 1$, which is parallel to the floor. We deal first with the terms relating to the viscosity function, we have that

$$\begin{aligned}r\frac{\partial}{\partial s}\left(\frac{v_\sigma}{r}\right)\Bigg|_{z=h} &= \frac{1}{\alpha}\left[r\frac{\partial}{\partial r}\left(\frac{v_\sigma}{r}\right) + h_r'\frac{\partial v}{\partial z}\right]\Bigg|_{z=h} \\ &= \frac{1}{\alpha}\left[r\frac{\partial}{\partial s}\left(\frac{v_\sigma}{r}\right) + \frac{(1-\mathcal{Z})h_\mathcal{R}'}{h}\frac{\partial v}{\partial \mathcal{Z}}\right]\Bigg|_{\mathcal{Z}=1} = \frac{\dot{\gamma}_\sigma}{\alpha}\Bigg|_{\mathcal{Z}=1},\end{aligned}$$

where

$$\dot{\gamma}_\sigma = \mathcal{R}\frac{\partial}{\partial \mathcal{R}}\left(\frac{v_\sigma}{\mathcal{R}}\right).$$

It follows directly that

$$\mu_\sigma = \begin{cases}\mu_{\text{yield}}, & |\dot{\gamma}_\sigma| \le \alpha\mathrm{Bn}\,\mu_{\text{yield}}^{-1}, \\ 1+\alpha\mathrm{Bn}(1-\mu_{\text{yield}}^{-1})|\dot{\gamma}_\sigma|^{-1}, & |\dot{\gamma}_\sigma| > \alpha\mathrm{Bn}\,\mu_{\text{yield}}^{-1}.\end{cases}$$

Having addressed these terms, we proceed to map the interfacial condition (A.3) from $r$-$z$ space to $\mathcal{R}$-$\mathcal{Z}$ space. After some algebraic manipulation, and noting that a number of the terms cancel with one another, the following is obtained

$$\begin{aligned}&\mathrm{Bo}\left[-\frac{\mu_\sigma}{(a_\mathrm{r} h)^2}\frac{\partial^2 v}{\partial \mathcal{Z}^2} + \mathcal{D}\mu_\sigma\frac{\partial}{\partial \mathcal{R}}\left[\mathcal{R}\frac{\partial}{\partial \mathcal{R}}\left(\frac{v}{\mathcal{R}}\right)\right]\right]\Bigg|_{\mathcal{Z}=1} \\ &\quad+\mathrm{Bo}\,\mu_\sigma\left\{2\frac{h_\mathcal{R}'}{h}\frac{\partial^2 v}{\partial \mathcal{R}\partial \mathcal{Z}} - \left(\frac{h_\mathcal{R}'}{h}\right)^2\frac{\partial^2 v}{\partial \mathcal{Z}^2} + \left[\frac{h_\mathcal{R}'}{\mathcal{R}h} + \frac{h_{\mathcal{R}\mathcal{R}}''}{h} - 2\left(\frac{h_\mathcal{R}'}{h}\right)^2\right]\right. \\ &\quad\left.\times\frac{\partial v}{\partial \mathcal{Z}}\right\}\Bigg|_{\mathcal{Z}=1} \\ &\quad-\mathrm{Bo}(\mu_\sigma+\mathcal{D}\mu_\sigma)\frac{a_\mathrm{r}^2 h_\mathcal{R}' h_{\mathcal{R}\mathcal{R}}''}{\alpha^2}\mathcal{R}\frac{\partial}{\partial \mathcal{R}}\left(\frac{v}{\mathcal{R}}\right)\Bigg|_{\mathcal{Z}=1} \\ &= \frac{\alpha}{h}\left\{[1+(a_\mathrm{r} h_\mathcal{R}')^2]\frac{\partial v}{\partial \mathcal{Z}} - a_\mathrm{r}^2 h h_\mathcal{R}'\mathcal{R}\frac{\partial}{\partial \mathcal{R}}\left(\frac{v}{\mathcal{R}}\right)\right\}\Bigg|_{\mathcal{Z}=1}.\end{aligned}$$

Collecting like terms, making use of the definition of the bulk shear rate (defined as $\dot{\gamma}$ in Section 2.3), rearranging, and noting that now $\mathcal{D}\mu_\sigma = |\dot{\gamma}_\sigma|(\mu_\sigma)'_{|\dot{\gamma}_\sigma|}$, such that $\mu_\sigma + \mathcal{D}\mu_\sigma = (|\dot{\gamma}_\sigma|\mu_\sigma)'_{|\dot{\gamma}_\sigma|}$, we then arrive at (11d):

$$\begin{aligned}&\left[a_\mathrm{r}^2 h\alpha\frac{\partial v}{\partial \mathcal{Z}} + \mathrm{Bo}\,\mu_\sigma\frac{\partial^2 v}{\partial \mathcal{Z}^2} - \mathrm{Bo}(a_\mathrm{r} h)^2|\dot{\gamma}_\sigma|(\mu_\sigma)'_{|\dot{\gamma}_\sigma|}\frac{\partial \dot{\gamma}}{\partial \mathcal{R}}\right]\Bigg|_{\mathcal{Z}=1} \\ &= \mathrm{Bo}\,a_\mathrm{r}^2\mu_\sigma\left(\beta_1\frac{\partial v}{\partial \mathcal{Z}} - \beta_2\frac{\partial^2 v}{\partial \mathcal{Z}^2} + 2\beta_3\frac{\partial^2 v}{\partial \mathcal{R}\partial \mathcal{Z}}\right)\Bigg|_{\mathcal{Z}=1} \\ &\quad+a_\mathrm{r}^4 h\beta_3\left[\alpha\left(\dot{\gamma} - \frac{h_\mathcal{R}'}{h}\frac{\partial v}{\partial \mathcal{Z}}\right) - \frac{\mathrm{Bo}\,h_{\mathcal{R}\mathcal{R}}''(|\dot{\gamma}_\sigma|\mu_\sigma)'_{|\dot{\gamma}_\sigma|}}{\alpha^2}\dot{\gamma}\right]\Bigg|_{\mathcal{Z}=1},\end{aligned} \tag{A.4}$$

where the $\beta_i$'s are as defined in Section 2.2.

## Appendix B. The SOR scheme inclusive of curvature and non-Newtonian effects

Here we outline the details of how the finite difference scheme detailed in Section 3 is adapted to account for the effects of both interfacial curvature and a non-Newtonian surface viscosity.

We begin by expressing (10) in terms of second-order accurate finite differences, we then isolate the $V_{i,j}$ terms and define the SOR scheme

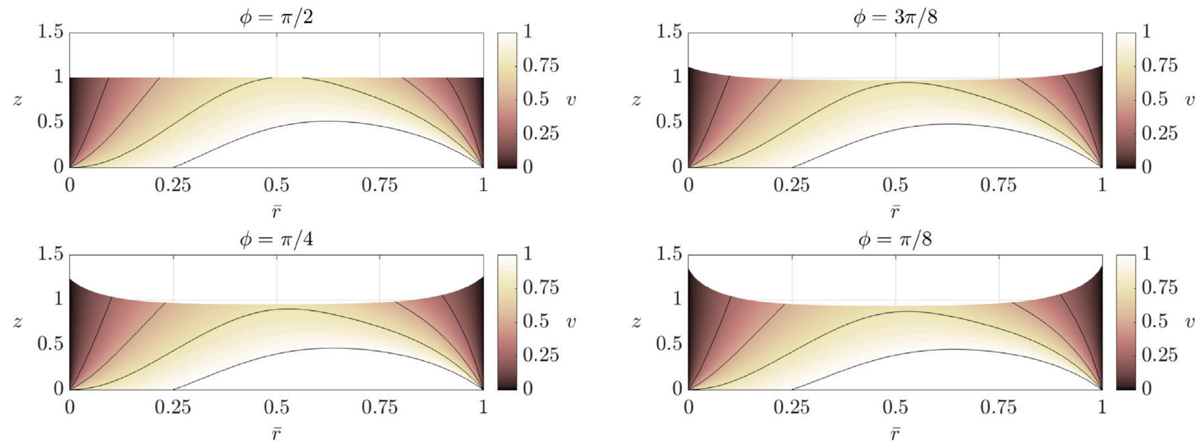


**Fig. C.15.** Plots of the azimuthal velocity component for increasing values of $\phi$. The contact angle decreases from left to right and down the page. In all cases the aspect ratio, Boussinesq number, and dimensionless capillary number are fixed; $a_r = 0.25$, $\mathrm{Bo} = 0.0625$, $\lambda = 0.1$.

accordingly

$$
\begin{aligned}
V_{i,j}^{k+1} = (1-\omega)V_{i,j}^{k} &+ \omega \frac{(a_r\delta_{\mathcal{Z}} h_i)^2 \mathcal{R}_i[(2\mathcal{R}_i+\delta_{\mathcal{R}})V_{i+1,j}^{k} + (2\mathcal{R}_i-\delta_{\mathcal{R}})V_{i-1,j}^{k+1}]}{2\{2[\delta_{\mathcal{R}}^2\mathcal{A}_{i,j} + (a_r\delta_{\mathcal{Z}}h_i)^2]\mathcal{R}_i^2 + (a_r\delta_{\mathcal{R}}\delta_{\mathcal{Z}}h_i)^2\}} \\
&+ \omega \frac{(\delta_{\mathcal{R}}\mathcal{R}_i)^2[(2\mathcal{A}_{i,j} - a_r^2\delta_{\mathcal{Z}}\mathcal{B}_{i,j})V_{i,j+1}^{k} + (2\mathcal{A}_{i,j} + a_r^2\delta_{\mathcal{Z}}\mathcal{B}_{i,j})V_{i,j-1}^{k+1}]}{2\{2[\delta_{\mathcal{R}}^2\mathcal{A}_{i,j} + (a_r\delta_{\mathcal{Z}}h_i)^2]\mathcal{R}_i^2 + (a_r\delta_{\mathcal{R}}\delta_{\mathcal{Z}}h_i)^2\}} \\
&+ \omega \frac{a_r^2\delta_{\mathcal{R}}\delta_{\mathcal{Z}}\mathcal{R}_i^2\mathcal{Z}_j h_i(h'_{\mathcal{R}})_i(V_{i+1,j-1}^{k+1} + V_{i-1,j+1}^{k+1} - V_{i+1,j+1}^{k} - V_{i-1,j-1}^{k+1})}{2\{2[\delta_{\mathcal{R}}^2\mathcal{A}_{i,j} + (a_r\delta_{\mathcal{Z}}h_i)^2]\mathcal{R}_i^2 + (a_r\delta_{\mathcal{R}}\delta_{\mathcal{Z}}h_i)^2\}},
\end{aligned}
$$

where

$$
\begin{aligned}
\mathcal{A}_{i,j} &= 1 + [a_r\mathcal{Z}_j(h'_{\mathcal{R}})_i]^2, \\
\mathcal{B}_{i,j} &= \{\mathcal{R}_i^{-1}h(h'_{\mathcal{R}})_i + h_i(h''_{\mathcal{R}\mathcal{R}})_i - 2[(h'_{\mathcal{R}})^2]_i\}\mathcal{Z}_j.
\end{aligned}
$$

In the instance when $h = 1$, i.e., the interface is planar in nature, the expression for $V_{i,j}^{k+1}$ collapses identically to that in (13), as is required.

We now need to apply exactly the same ideas to the surface boundary condition (11d). It proves useful to collect like terms and express the condition in the following manner

$$
a_r^2\mathcal{S}_1\frac{\partial v}{\partial \mathcal{Z}} + \mathrm{Bo}\,\mathcal{S}_2\frac{\partial^2 v}{\partial \mathcal{Z}^2} - a_r^2\mathcal{S}_3\frac{\partial^2 v}{\partial\mathcal{R}\partial\mathcal{Z}} - a_r^4\mathcal{S}_4\dot{\gamma} - \mathrm{Bo}\,a_r^2\mathcal{S}_5\frac{\partial\dot{\gamma}}{\partial\mathcal{R}} = 0, \tag{B.1}
$$

where

$$
\begin{aligned}
&\mathcal{S}_1 = h\alpha - \mathrm{Bo}\,\mu_\sigma\beta_1 + a_r^2h'_{\mathcal{R}}\alpha\beta_3, \qquad \mathcal{S}_2 = \mu_\sigma(1+a_r^2\beta_2), \qquad \mathcal{S}_3 = 2\mathrm{Bo}\,\mu_\sigma\beta_3, \\
&\mathcal{S}_4 = h\beta_3[\alpha - \mathrm{Bo}\,h''_{\mathcal{R}\mathcal{R}}\alpha^{-2}(\dot{\gamma}_\sigma\mu_\sigma)'_{\dot{\gamma}_\sigma}], \qquad \mathcal{S}_5 = h^2\dot{\gamma}_\sigma(\mu_\sigma)'_{\dot{\gamma}_\sigma}.
\end{aligned}
$$

In the limit as $h \to 1$, then $\mathcal{S}_1 \to 1$, $\mathcal{S}_2 \to \mu_\sigma$, $\mathcal{S}_3 \to 0$, $\mathcal{S}_4 \to 0$, and $\mathcal{S}_5 \to \dot{\gamma}_\sigma(\mu_\sigma)'_{\dot{\gamma}_\sigma}$. Thus the third and fourth terms appear only as a consequence of interface curvature whereas the fifth term appears only due to the non-Newtonian description of the surface viscosity.

Making use of second-order accurate finite difference expressions for each of the $\mathcal{R}$-derivatives associated with $\mathcal{S}_3 - \mathcal{S}_5$, and given that $V_{1,N_{\mathcal{Z}}+1} = V_{N_{\mathcal{R}}+1,N_{\mathcal{Z}}+1} \equiv 0$, (B.1) can be expressed as such

$$
\begin{aligned}
&(c_0^{(1)}\delta_{\mathcal{Z}}a_r^2\mathcal{S}_1 + c_0^{(2)}\mathrm{Bo}\,\mathcal{S}_2)V_{i,N_{\mathcal{Z}}+1}^{k+1} = \\
&\quad - c_{-p}^{(2)}\mathrm{Bo}\,\mathcal{S}_2V_{i,N_{\mathcal{Z}}+1-p}^{k+1} - \sum_{l=1}^{l=p-1}(c_{-l}^{(1)}\delta_{\mathcal{Z}}a_r^2\mathcal{S}_1 + c_{-l}^{(2)}\mathrm{Bo}\,\mathcal{S}_2)V_{i,N_{\mathcal{Z}}+1-l}^{k+1} \\
&\quad + (a_r\delta_{\mathcal{Z}})^2\mathcal{S}_3\left[\frac{c_0^{(1)}V_{i+1,N_{\mathcal{Z}}+1}^{k} + c_{-1}^{(1)}V_{i+1,N_{\mathcal{Z}}}^{k} + \sum_{l=2}^{l=p-1}c_{-l}^{(1)}V_{i+1,N_{\mathcal{Z}}+1-l}^{k+1}}{2\delta_{\mathcal{R}}\delta_{\mathcal{Z}}}\right] \\
&\quad - (a_r\delta_{\mathcal{Z}})^2\mathcal{S}_3\left[\frac{c_0^{(1)}V_{i-1,N_{\mathcal{Z}}+1}^{k+1} + c_{-1}^{(1)}V_{i-1,N_{\mathcal{Z}}}^{k+1} + \sum_{l=2}^{l=p-1}c_{-l}^{(1)}V_{i-1,N_{\mathcal{Z}}+1-l}^{k+1}}{2\delta_{\mathcal{R}}\delta_{\mathcal{Z}}}\right] \\
&\quad + a_r^2(a_r\delta_{\mathcal{Z}})^2\mathcal{S}_4\left[\frac{V_{i+1,N_{\mathcal{Z}}+1}^{k} - V_{i-1,N_{\mathcal{Z}}+1}^{k+1}}{2\delta_{\mathcal{R}}} - \frac{V_{i,N_{\mathcal{Z}}+1}^{k}}{\mathcal{R}_i}\right] \\
&\quad + \mathrm{Bo}(a_r\delta_{\mathcal{Z}})^2\mathcal{S}_5\left[\frac{V_{i+1,N_{\mathcal{Z}}+1}^{k} - 2V_{i,N_{\mathcal{Z}}+1}^{k} + V_{i-1,N_{\mathcal{Z}}+1}^{k+1}}{\delta_{\mathcal{R}}^2} - \frac{(V_{i+1,N_{\mathcal{Z}}+1}^{k} - V_{i-1,N_{\mathcal{Z}}+1}^{k+1})}{2\delta_{\mathcal{R}}\mathcal{R}_i} + \frac{V_{i,N_{\mathcal{Z}}+1}^{k}}{\mathcal{R}_i^2}\right],
\end{aligned} \tag{B.2}
$$

for $2 \le i \le N_{\mathcal{R}}$. In the planar Newtonian analysis the quantity $V_{i,N_{\mathcal{Z}}+1}$ depends only on predetermined quantities. Thus we are able to specify the condition (14) outside of the SOR iterative procedure, i.e., the condition is free from superscripts given that everything is evaluated at the $(k+1)^{\mathrm{st}}$ step. However, in both the non-planar and non-Newtonian analyses we obtain an implicit expression for $V_{i,N_{\mathcal{Z}}+1}$ in terms of both itself and $V_{i+1,N_{\mathcal{Z}}+1}$. Thus, in order to effectively implement this condition, we evaluate the implicit terms at the previous iteration, as noted above. Given the stringent convergence criteria that we have outlined in Section 3, we argue that this approximation is entirely justified. Indeed, testing in the planar Newtonian case, where all of the terms that appear on the right-hand side of (14) are evaluated at the $k$th iteration, as opposed to the $(k+1)$st iteration, produces no difference in the accuracy of the results presented in Table 1.

In the instances when $\mu_\sigma = \mu_\sigma(\dot{\gamma}_\sigma)$, we again approximate $|\dot{\gamma}_\sigma|$ using second-order accurate finite differences as per (B.2). Additional care also needs to be taken when one considers the application of the biviscosity model. In these instances, to effectively employ the condition (B.2), we first multiply (B.1) throughout by $|\dot{\gamma}_\sigma|$. This ensures that we avoid the numerical challenges associated with raising vanishingly small values to a negative exponent. We have omitted the details of this step in order to not overly complicate what is already a reasonably lengthy analysis.

## Appendix C. Hydrophilic results

Here we present results equivalent to those appearing in Section 4.1 for the cases when the fluid under consideration is hydrophilic in nature, i.e., the contact angle is less than $\phi = \pi/2$. As the contact angle decreases, the effect of the no-slip boundary condition appears to penetrate slightly further into the flow domain (see Fig. C.15). However, the maximum value of the surface velocity is almost unchanged upon increasing $\lambda$, even in the most extreme case when $\phi = \pi/8$ (see Fig. C.16). In addition to this, the variation of the radial location at which the maximum surface velocity is attained is again almost unchanged. As per the hydrophobic case, both $\max(v_\sigma)$ and $\bar{r}_{\max}$ diminish as the Boussinesq number increases. However, unlike the hydrophobic case, these quantities are largely unaffected by a reduction in the contact angle. These results suggest that, away from the walls, hydrophilicity

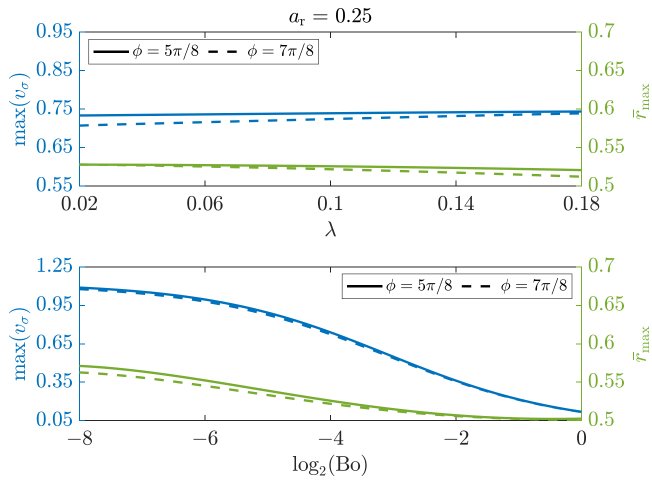


**Fig. C.16.** In both figures we plot the variation of $\max(v_\sigma)$ (blue) and $\bar{r}_{\max}$ (green). In the top figure, the Boussinesq number is fixed such that $\mathrm{Bo} = 0.0625\,(\implies \log_2(\mathrm{Bo}) = -4)$, whereas in the bottom figure the dimensionless capillary length is fixed such that $\lambda = 0.1$.

does not strongly affect the flow field. These findings are in direct contrast to the hydrophobic results we present in Section 4.1.

## Data availability

No data was used for the research described in the article.

## References

[1] S. Cheng, Z. Wu, A microfluidic, reversibly stretchable, large-area wireless strain sensor, Adv. Funct. Mater. 21 (2011) 2282–2290.
[2] K. Doudrick, S. Liu, E.M. Mutunga, K.L. Klein, V. Damle, K.K. Varanasi, K. Rykaczewski, Different shades of oxide: From nanoscale wetting mechanisms to contact printing of gallium-based liquid metals, Langmuir 30 (2014) 6867–6877.
[3] M.D. Dickey, Stretchable and soft electronics using liquid metals, Adv. Mater. 29 (2017) 1606425.
[4] M.D. Bartlett, M.D. Dickey, A.T. Ohta, K. Kalantar-Zadeh, Let it flow: Emergence of liquid metals, Adv. Funct. Mater. 34 (2024) 2405143.
[5] C.B. Eaker, I.D. Joshipura, L.R. Maxwell, J. Heikenfeld, M.D. Dickey, Electrowetting without external voltage using paint-on electrodes, Lab Chip 17 (2017) 1069–1075.
[6] M.D. Dickey, Emerging applications of liquid metals featuring surface oxides, ACS Appl. Mater. Interfaces 6 (2014) 18369–18379.
[7] W. Yang, R. Yang, Y. Yao, Z. Gao, H. Zhang, Effects of surface oxide layer on the impact dynamic behavior of molten aluminum droplets, Phys. Fluids 35 (2014) 013109.
[8] X. Zhao, S. Xu, J. Liu, Surface tension of liquid metal: role, mechanism and application, Front. Energy 11 (2017) 535–567.
[9] K. Patouillet, L. Davoust, O. Doche, Deal–Grove model revisited for a new insight into the oxidation of molten aluminum alloy: The A356 alloy, as a model system, AIChE J. 67 (2021) e17230.
[10] H. Ragelle, M.W. Tibbitt, S.Y. Wu, M.A. Castillo, G.Z. Cheng, S.P. Gangadharan, D.G. Anderson, M.J. Cima, R. Langer, Surface tension-assisted additive manufacturing, Nat. Commun. 9 (2018) 31184.
[11] J. Fu, Z. Hu, X. Song, W. Zhai, Y. Long, H. Li, M. Fu, Micro selective laser melting of NiTi shape memory alloy: defects, microstructures and thermal/mechanical properties, Opt. Laser Technol. 131 (2020) 106374.
[12] F. Han, S. Gu, A. Klimas, N. Zhao, Y. Zhao, S.C. Chen, Three-dimensional nanofabrication via ultrafast laser patterning and kinetically regulated material assembly, Science 378 (2020) 325–1331.
[13] G. Li, M. Parmar, D.W. Lee, An oxidized liquid metal-based microfluidic platform for tunable electronic device applications, Lab Chip 15 (2015) 766–775.
[14] K. Khoshmanesh, S.Y. Tang, J.Y. Zhu, S. Schaefer, A. Mitchell, K. Kalantar-zadeha, M.D. Dickey, Liquid metal enabled microfluidics, Lab Chip 17 (2017) 974–993.
[15] L. Davoust, Y.L. Huang, S.H. Chang, Shearing of a stratified layer of amphiphilic (bio)molecules, Surf. Sci. 603 (2009) 2777–2788.
[16] K. Patouillet, L. Davoust, Between no slip and free slip: A new boundary condition for the surface hydrodynamics of a molten metal, Chem. Eng. Sci. 231 (2021) 116328.
[17] J. Delacroix, L. Davoust, Electrical activity of the hartmann layers relative to surface viscous shearing in an annular magnetohydrodynamic flow, Phys. Fluids 26 (2014) 037102.
[18] J. Delacroix, L. Davoust, K. Patouillet, Low Rm magnetohydrodynamics as a means of measuring the surface shear viscosity of a liquid metal: A first attempt on galinstan, Rev. Sci. Instrum. 89 (2018) 015103.
[19] J. Delacroix, L. Davoust, K. Patouillet, Viscosimetry of a non-Newtonian interface: The interesting role of MHD, Magnetohydrodynamics 56 (2020) 177–186.
[20] N.O. Jaensson, P.D. Anderson, J. Vermant, Computational interfacial rheology, J. Non-Newton. Fluid Mech. 290 (2021) 104507.
[21] W.D. Harkins, R.J. Meyers, Viscosity of monomolecular films, Nature 140 (1937) 465.
[22] R.J. Mannheimer, R.S. Schechter, An improved apparatus and analysis for surface rheological measurements, J. Colloid Interface Sci. 32 (1970) 195–211.
[23] A.J. Pintar, A.B. Israel, D.T. Wasan, Interfacial shear viscosity phenomena in solutions of macromolecules, J. Colloid Interface Sci. 37 (1970) 52–67.
[24] J.M. Lopez, A.H. Hirsa, Direct determination of the dependence of the surface shear and dilatational viscosities on the thermodynamic state of the interface: Theoretical foundations, J. Colloid Interface Sci. 206 (1998) 231–239.
[25] A.H. Hirsa, J.M. Lopez, R. Miraghaie, Determination of surface shear viscosity via deep-channel flow with inertia, J. Fluid Mech. 470 (2002) 135–149.
[26] J.M. Lopez, R. Miraghaie, A.H. Hirsa, Non-Newtonian behavior of an insoluble monolayer: effects of inertia, J. Colloid Interface Sci. 248 (2002) 103–110.
[27] L. Drazek, J.F. Legrand, L. Davoust, A first attempt to enhance the 2-D single-crystal growth of a protein at an air/water interface from hydrodynamics, J. Cryst. Growth 275 (2005) e1467–e1472.
[28] L. Davoust, J.L. Achard, L. Drazek, Low-to-moderate Reynolds number swirling flow in an annular channel with a rotating end wall, Phys. Rev. E 91 (2015) 023019.
[29] P.T. Underhill, A.H. Hirsa, J.M. Lopez, Modelling steady shear flows of Newtonian liquids with non-Newtonian interfaces, J. Fluid Mech. 814 (2017) 23.
[30] A. Raghunandan, A.H. Hirsa, P.T. Underhill, J.M. Lopez, Predicting steady shear rheology of condensed-phase monomolecular films at the air-water interface, Phys. Rev. Lett. 121 (2018) 164502.
[31] C. Picard, L. Davoust, Resonance frequencies of meniscus waves as a physical mechanism for a DNA biosensor, Langmuir 23 (2007) 1394–1402.
[32] K. Patouillet, L. Davoust, O. Doche, J. Delacroix, Mannheimer and schechter model revisited: Viscosimetry of a (non-)Newtonian and curved interface, Phys. Rev. Fluid 4 (2019) 054002.
[33] J.C. Slattery, L. Sagis, E.S. Oh, Interfacial Transport Phenomena, second ed., Springer Nature, 2007.
[34] K. Patouillet, Characterisation of the Oxidized Surface of Molten Metal: Curvature Effects, Non-Newtonian Behaviour, and Benefits of Magnetohydrodynamics (Ph.D. thesis), Université Grenoble Alpes, 2020.
[35] E.J. O'Donovan, R.I. Tanner, Numerical study of the Bingham squeeze film problem, J. Non-Newton. Fluid Mech. 15 (1984) 75–83.
[36] I.A. Frigaard, C. Nouar, On the usage of viscosity regularisation methods for visco-plastic fluid flow computation, J. Non-Newton. Fluid Mech. 127 (2005) 1–26.
[37] N.J. Balmforth, I.A. Frigaard, G. Ovarlez, Yielding to stress: Recent developments in viscoplastic fluid mechanics, Annu. Rev. Fluid Mech. 46 (2009) 121–146.
[38] N.J. Balmforth, D.R. Hewitt, The implications of a fluid yield stress, J. Fluid Mech. 1011 (2025) 1–66, P1.
[39] H. Rahman, S.M. Taghavi, Viscoplastic flows in superhydrophobic channels with oriented grooves: From anisotropic slip to secondary flow, J. Non-Newton. Fluid Mech. 326 (2024) 105203.
[40] B. Samanta, M. Kaushal, G. Das, S. Ray, A numerical investigation of laminar planar hydraulic jump in Herschel-Bulkley fluid, J. Non-Newton. Fluid Mech. 333 (2024) 105325.
[41] I. Siqueira, R.L. Thompson, M.S. Carvalho, P. de Souza Mendes, Slot coating of viscoplastic materials: A computational study of the effects of viscoplasticity on the flow dynamics and low-flow limit, J. Non-Newton. Fluid Mech. 327 (2024) 105222.
[42] A. Syrakos, E. Gryparis, G.C. Georgiou, A revisit of the development of viscoplastic flow in pipes and channels, J. Non-Newton. Fluid Mech. 334 (2024) 105341.
[43] T.C. Papanastasiou, Flows of materials with yield, J. Rheol. 31 (1987) 385–404.
[44] M. Abramowitz, I.A. Stegun, Handbook of Mathematical Functions, Dover, 1970.
[45] E.A. Muravleva, Finite-difference schemes for the computation of viscoplastic medium flows in a channel, Math. Models Comput. Simul. 1 (2009) 768–779.
[46] L. Muravlevaa, E. Muravleva, G.C. Georgiouc, E. Mitsoulis, Numerical simulations of cessation flows of a Bingham plastic with the augmented Lagrangian method, J. Non-Newton. Fluid Mech. 165 (2010) 544–550.
[47] L. Fusi, A. Farina, Bingham fluid with viscosity and yield stress depending on the density, Int. J. Non-Linear Mech. 199 (2020) 103356.

[48] L. Fusi, A finite difference scheme for the unsteady planar motion of a Bingham fluid, J. Non-Newton. Fluid Mech. 299 (2022) 104702.
[49] M.F. Tomé, G.S. Paulo, F.T. Pinho, M.A. Alves, Numerical solution of the PTT constitutive equation for unsteady three-dimensional free surface flows, J. Non-Newton. Fluid Mech. 165 (2010) 247–262.
[50] G.S. Paulo, C. Viezel, L.L. Ferrás, A robust finite difference method for confined and free surface flows with slip at the wall, J. Non-Newton. Fluid Mech. 321 (2023) 105127.
[51] P.P. Dabrowski, Boundary-Layer Flows in Non-Newtonian Fluids (Ph.D. thesis), The University of Adelaide, 2009.
[52] C.R. Beverly, R.I. Tanner, Numerical analysis of extrudate swell in viscoelastic materials with yield stress, J. Rheol. 33 (1989) 989–1009.
[53] O. Turana, N. Chakrabortya, R.J. Poole, Laminar natural convection of bingham fluids in a square enclosure with differentially heated side walls, J. Non-Newton. Fluid Mech. 165 (2010) 901–913.